Volume 640 Issue 8060, 24 April 2025

Spatial awareness

The complex ecosystem of cells and blood vessels that make up the tumour microenvironment exerts a strong influence over how tumours form, grow and respond to treatment. Aspects of the microenvironment, such as the distribution and location of immune cells, can be used to predict disease outcomes, and in this week's issue, Cheng Sun and colleagues capitalize on this to create an image-based scoring methodology that can predict whether liver cancer is likely to recur after surgery. The researchers focused on the most common form of liver cancer, hepatocellular carcinoma, which has a high recurrence rate. They found that the spatial distribution of immune cells called natural killer cells, and five genes expressed by those cells, was linked to improved outcomes after surgery. This allowed the team to develop the tumour immune microenvironment spatial (TIMES) score, a spatial-profiling system using artificial intelligence that can predict recurrence of liver cancer based on where in the microenvironment the genes are expressed. — show less

Cover image: Cheng Sun.

Subscribe

Table of Contents

This Week

News in Focus

Article

Spatial immune scoring system predicts hepatocellular carcinoma recurrence

https://doi.org/10.1038/s41586-025-08668-x

Received: 18 March 2023

Accepted: 17 January 2025

Published online: 12 March 2025

Check for updates

Gengjie Jia[1,2,3,4,12], Peiqi He[1,2,3,12], Tianli Dai[1,2,3,12], Denise Goh[5,12], Jiabei Wang[1,3], Mengyuan Sun[1,2,3], Felicia Wee[5], Fuling Li[1,2,3], Jeffrey Chun Tatt Lim[5], Shuxia Hao[4], Yao Liu[1,3], Tony Kiat Hon Lim[1,6], Nye-Thane Ngo[6], Qingping Tao[1,2,3], Wei Wang[1,2,3], Ahitsham Umar[1,2], Björn Nashan[1], Yongchang Zhang[7], Chen Ding[8], Joe Yeong[5,9,10,11]✉, Lianxin Liu[1]✉ & Cheng Sun[1,2]✉

Given the high recurrence rates of hepatocellular carcinoma (HCC) post-resection[1–3], improved early identification of patients at high risk for post-resection recurrence would help to improve patient outcomes and prioritize healthcare resources[4–6]. Here we observed a spatial and HCC recurrence-associated distribution of natural killer (NK) cells in the invasive front and tumour centre from 61 patients. Using extreme gradient boosting and inverse-variance weighting, we developed the tumour immune microenvironment spatial (TIMES) score based on the spatial expression patterns of five biomarkers (SPON2, ZFP36L2, ZFP36, VIM and HLA-DRB1) to predict HCC recurrence risk. The TIMES score (hazard ratio = 88.2, $P < 0.001$) outperformed current standard tools for patient risk stratification including the TNM and BCLC systems. We validated the model in 231 patients from five multicentred cohorts, achieving a real-world accuracy of 82.2% and specificity of 85.7%. The predictive power of these biomarkers emerged through the integration of their spatial distributions, rather than individual marker expression levels alone. In vivo models, including NK cell-specific *Spon2*-knockout mice, revealed that SPON2 enhances IFNγ secretion and NK cell infiltration at the invasive front. Our study introduces TIMES, a publicly accessible tool for predicting HCC recurrence risk, offering insights into its potential to inform treatment decisions for early-stage HCC.

HCC is the third-leading cause of cancer-related mortality worldwide, with a recurrence rate of approximately 70% post-resection[1–3]. Accurate prediction of HCC recurrence risk is beneficial for optimizing clinical management and improving patient outcomes. Current prognostic tools, such as staging systems and molecular biomarkers, leave room for improvement in accurately predicting HCC recurrence, especially for early-stage HCC[4–6]. One potential reason is that these approaches do not adequately account for the spatial heterogeneity and interactions within the tumour microenvironment (TME)[7,8].

The TME in HCC is characterized by substantial spatial heterogeneity, with varying compositions of immune cells across different tumour regions[1]. NK cells of the innate immune system have emerged as potential prognostic indicators in early-stage HCC[9–13]. Increased NK cell activity and infiltration, particularly within the tumour, have been associated with improved survival outcomes[9–20]. Nevertheless, the precise spatial distribution of NK cells within tumours of patients and its potential effect on prognosis have not been extensively characterized[21]. Furthermore, the spatial distribution of immune cells within tumours has been linked to metastatic recurrence[22–25], suggesting that the localization of immune cells across tumour regions may influence HCC recurrence[26,27]. Despite this, current clinical strategies primarily rely on histopathological stratification of tumour characteristics without considering the spatial context of intratumoural immune cell phenotypes, which requires whole-slide image (WSI) analysis and artificial intelligence-driven spatial profiling.

To address these limitations and harness the potential of spatial immune profiling, we integrated spatial transcriptomics, proteomics and multiplex immunohistochemistry (mIHC) data with artificial intelligence-driven analysis. This approach enabled us to delineate the spatial distribution of NK cells in the invasive front (IF) and tumour centre (TC) of HCC tissues and its correlation with post-resection recurrence. Building on these findings, we sought to develop and validate a TIMES scoring system to predict HCC recurrence risk based on the spatial expression patterns of key immune markers. In addition, we

[1]Department of Hepatobiliary Surgery, Anhui Provincial Clinical Research Center for Hepatobiliary Diseases, Anhui Province Key Laboratory of Hepatopancreatobiliary Surgery, The First Affiliated Hospital of University of Science and Technology of China (USTC), University of Science and Technology of China, Hefei, China. [2]Chinese Academy of Sciences Key Laboratory of Innate Immunity and Chronic Disease, Key Laboratory of Immune Response and Immunotherapy, Institute of Immunology, School of Basic Medical Sciences, Division of Life Sciences and Medicine, University of Science and Technology of China, Hefei, China. [3]Clinical Research Hospital of Chinese Academy of Sciences, University of Science and Technology of China, Hefei, China. [4]Genome Analysis Laboratory of the Ministry of Agriculture and Rural Affairs, Agricultural Genomics Institute at Shenzhen, Chinese Academy of Agricultural Sciences, Shenzhen, China. [5]Institute of Molecular and Cell Biology (IMCB), Agency for Science Technology and Research (A*STAR), Singapore, Singapore. [6]Duke-NUS Medical School, Singapore, Singapore. [7]Hunan Cancer Hospital, The Affiliated Cancer Hospital of Central South University, Changsha, China. [8]State Key Laboratory of Genetic Engineering and Collaborative Innovation Center for Genetics and Development, School of Life Sciences, Institutes of Biomedical Sciences, Human Phenome Institute, Fudan University, Shanghai, China. [9]Department of Anatomical Pathology, Singapore General Hospital, Singapore, Singapore. [10]Singapore Immunology Network (SIgN), Agency for Science Technology and Research (A*STAR), Singapore, Singapore. [11]Cancer Science Institute, National University of Singapore, Singapore, Singapore. [12]These authors contributed equally: Gengjie Jia, Peiqi He, Tianli Dai, Denise Goh. ✉e-mail: yeongps@imcb.a-star.edu.sg; liulx@ustc.edu.cn; charless@ustc.edu.cn

elucidated the functional role of SPON2$^+$ NK cells in HCC progression and recurrence through in vitro and in vivo models, providing mechanistic insights into the observed prognostic patterns. By leveraging WSI analysis and artificial intelligence-driven spatial profiling, we have advanced HCC patient risk stratification beyond current clinical factors. The TIMES scoring system represents a step forwards in prognostic accuracy for HCC, and our functional studies illuminate the immunological underpinnings of HCC recurrence.

NK cells at the IF lowers recurrence

To analyse whether the spatial heterogeneity of immune cells affects HCC recurrence, we performed spatial transcriptomic analysis (10x Visium Gene Expression) of 76,599 spots from a discovery cohort of 17 patients with HCC, comprising 6 recurrent (REC) and 11 non-recurrent (non-REC) cases (Fig. 1a and Supplementary Tables 1–9). Unbiased clustering analysis segregated the whole tissue into three tissue compartments: adjacent stroma (AS), IF and TC. These compartments were confirmed through assessment by pathologists (Fig. 1b), reticulin staining and IHC staining of HCC markers (Extended Data Fig. 1a). Spatial uniform manifold approximation and projection (UMAP) clustering revealed high transcriptomic heterogeneity across compartments in both non-REC and REC HCC (Fig. 1c and Extended Data Fig. 1b,c).

Next, we characterized the abundance of NK cells, T cells, B cells and myeloid cells by calculating enrichment scores based on their respective gene markers (Fig. 1d). The most striking difference between the REC and non-REC HCC was the significantly higher enrichment scores of NK cells in the IF of non-REC HCC than of REC HCC ($P = 4.3 \times 10^{-4}$), suggesting that patients with increased NK cell infiltration in the IF have a lower recurrence risk. mIHC with WSI analysis on samples from 61 patients with HCC (30 REC and 31 non-REC) revealed enrichment of NK cells in the IF of non-REC HCC compared with REC HCC (Fig. 1e). The analysis identified three distinct NK cell populations: CD3$^-$CD56$^+$ ordinary NK ($P = 3.5 \times 10^{-2}$), CD3$^-$CD16$^+$CD56$^+$ cytotoxic NK ($P = 3.0 \times 10^{-3}$) and CD3$^-$CD57$^+$ mature NK ($P = 8.0 \times 10^{-4}$) cell populations were significantly enriched in the IF of non-REC HCC compared with REC HCC (Fig. 1f and Extended Data Fig. 1d,e).

To determine which NK cell subset is strongly associated with HCC prognosis, we compared the relationship between the three identified NK cell populations and disease-free survival (DFS). Samples were stratified into IF-NK^{high} and IF-NK^{low} subgroups according to the median IF density for each NK cell subtype. The IF-CD3$^-$CD57$^+$NK^{high} subgroup demonstrated significantly longer DFS than the IF-CD3$^-$CD57$^+$NK^{low} subgroup ($P = 6.6 \times 10^{-3}$; Fig. 1g and Supplementary Fig. 1). By contrast, no significant difference in DFS was observed between the high and low subgroups for the other two NK cell populations (Extended Data Fig. 1f,g). These findings suggest that CD3$^-$CD57$^+$ NK cells in the IF are the NK cell subset most closely associated with HCC recurrence risk.

Spatial gene patterns predict recurrence

To identify differentially expressed genes (DEGs) between CD3$^-$CD57$^+$ NK cells in non-REC and REC HCC, which could serve as predictive indicators of recurrence risk, we used the GeoMx Digital Spatial Profiler (DSP) Human Whole Transcriptome Atlas to assess 18,677 protein-coding human genes in CD3$^-$CD57$^+$ NK cell-enriched regions across the AS, IF and TC compartments of eight HCC tissues from the discovery cohort (Fig. 1h,i). Spatial analysis revealed 241 DEGs with distinct spatial patterns across the AS, IF and TC compartments in patients with non-REC versus REC (Fig. 2a,b and Supplementary Tables 10 and 11). Of these 241 DEGs, 23 were differentially expressed in NK cells compared with other immune cells, based on independent single-cell RNA sequencing (RNA-seq) data[28]. For each of these 23 DEGs, we constructed a generalized linear model using transcript counts at the IF and TC to evaluate their predictive capacity for recurrence outcome. Transcript counts at the AS were not integrated into the model, as the AS compartment was considered normal tissue and showed no significant differences in gene expression between REC and non-REC HCC. Five DEGs (*SPON2*, *ZFP36L2*, *ZFP36*, *VIM* and *HLA-DRB1*) achieved the highest prediction accuracies for recurrence (Fig. 2c,d, Supplementary Table 12 and Supplementary Figs. 2 and 3). Moreover, proteomics analysis[29–33] of HCC tissues from the discovery cohort (Supplementary Table 22) isolated by laser-capture microdissection, using liquid chromatography–tandem mass spectrometry (LC–MS/MS)[33], confirmed the differential protein expressions of these five DEGs between REC and non-REC HCC (Fig. 2e,f, Extended Data Fig. 2a–d and Supplementary Fig. 4). Of note, analyses of patients with HCC from The Cancer Genome Atlas (TCGA) database revealed that DFS and gene expression levels (only from the TC) of the five DEGs were not significantly different between non-REC and REC HCC (Extended Data Fig. 2e,f), underscoring the importance of spatial information of the five DEGs (biomarkers) in accurately predicting HCC recurrence.

TIMES system stratifies recurrence risk

To develop a predictive model based on the spatial information of the five DEGs, we first quantified the protein levels of the five biomarkers and CD57 by using mIHC in 61 patients with HCC (30 REC and 31 non-REC) from cohort 1 (Fig. 3a, Supplementary Tables 1 and 2 and Supplementary Fig. 5). High-resolution WSIs were obtained for each patient sample, with 100–600 tiles per slide based on tissue size. Biomarker expression was quantified in each tile at the IF and TC using InForm and HALO[34,35]. In the model development stage, we utilized the whole-slide mIHC data from these 61 patients to build and validate a machine learning model based on the extreme gradient boosting (XGBoost) algorithm for predicting HCC recurrence risks (Fig. 3b, Extended Data Fig. 3a and Supplementary Tables 13 and 14). We used repeated random splits of the data, using 75% ($n = 46$) for training and 25% ($n = 15$) for validation. On the validation set, the model achieved an area under the receiver operating characteristic curve (AUC) greater than 0.87 for each individual biomarker, indicating its high predictive accuracy (Supplementary Table 14).

To further enhance the potential clinical utility of the model, we designed a two-step scoring system based on the trained XGBoost models to integrate information from spatially diverse tissue tiles and multiple biomarkers (Fig. 3b). This approach generated an integrative score (known as TIMES score) for each patient, ranging from 0 to 1, with higher scores indicating greater HCC recurrence risk (see Methods; Supplementary Table 15). TIMES scores from REC tissues were significantly higher than those of non-REC tissues, with a median score difference of 0.375 ($P = 3.13 \times 10^{-13}$; Fig. 3c). The TIMES scoring system differentiated non-REC and REC tissues with an accuracy of 82.2% and a specificity of 85.7%. TIMES successfully stratified non-REC from REC tissues in both early and late HCC stages, outperforming Tumor Node Metastasis (TNM) and Barcelona Clinic Liver Cancer (BCLC) staging[36,37] (Fig. 3d and Extended Data Fig. 3b–d) and implying that TIMES surpassed traditional staging systems in stratifying recurrence risk, particularly in early-stage HCC.

To explore whether TIMES outperforms traditional recurrence-related clinical factors in predicting the risk of HCC recurrence, we compared its prognostic performance against 118 clinical factors in a validation cohort of 231 patients (Supplementary Table 16). Compared with the 118 clinical factors, TIMES had the strongest association with DFS ($P = 3.85 \times 10^{-14}$; Extended Data Fig. 3e). Multivariate regression analysis using 17 significant clinical factors ($P < 0.05$ in univariate regressions) as covariates further supported the strongest association of TIMES with prognosis outcome ($P = 3.82 \times 10^{-11}$; Extended Data Fig. 3f). Discriminant analysis also identified the TIMES score as the most discriminative variable in differentiating non-REC from REC HCC (Fig. 3e). Three multivariate models were constructed based on:

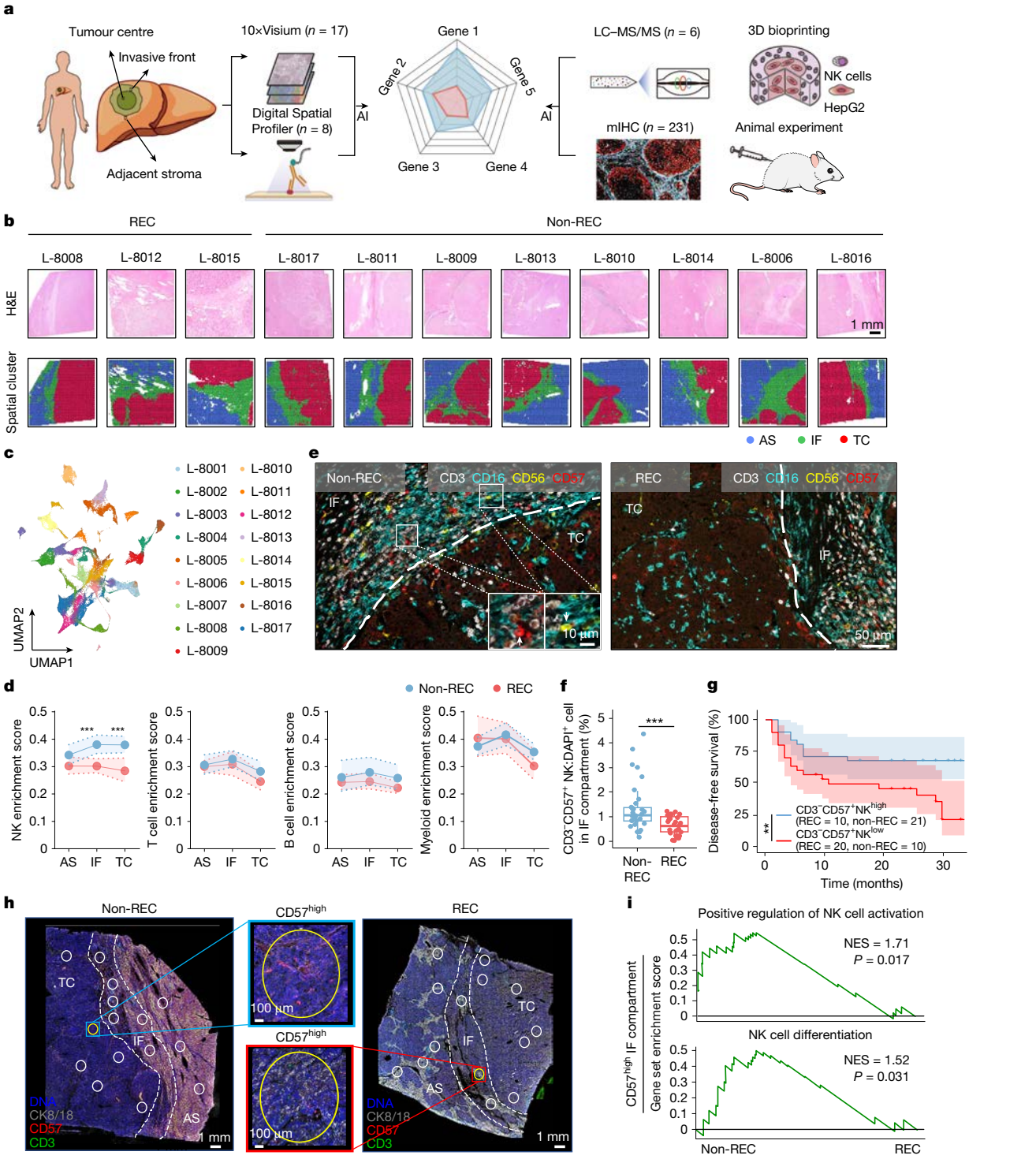

Fig. 1 | Spatial multi-omics analysis reveals associations between NK cell distribution and HCC recurrence. a, Study design. We conducted spatial profiling across the AS, IF and TC compartments (10x Visium and DSP). Artificial intelligence (AI) analysis identified five recurrence-associated genes, validated by LC–MS/MS proteomics. The TIMES scoring system was developed for HCC recurrence prediction, followed by 3D bioprinting and animal validation. **b**, Haematoxylin and eosin (H&E) images (top) and spatial clustering (bottom) in REC or non-REC HCC tissues. **c**, UMAP embedding of spatial transcriptome sequencing from 18 Visium samples (6 patients with REC, 11 patients with non-REC). **d**, Leukocyte gene-based enrichment. The shaded areas correspond to 95% confidence intervals and the central lines indicate means; non-REC ($n = 11$ patients) versus REC ($n = 6$ patients), unpaired two-tailed Welch's t-test: $P = 4.3 \times 10^{-4}$ (IF) and $P = 9.2 \times 10^{-4}$ (TC) for NK cells. **e**, mIHC staining of CD3, CD16, CD56 and CD57 in non-REC and REC tissues. **f**, $CD3^{-}CD57^{+}$ NK cell proportions at the IF between patients with non-REC ($n = 31$) and REC ($n = 30$). The boxplots show minima (0.19 non-REC and 0.18 REC), maxima (4.31 non-REC and 1.24 REC) and median (1.06 non-REC and 0.62 REC), with whiskers extending to the most extreme data points. Each dot represents the mean of all measurements per patient. Unpaired two-tailed Student's t-test: $P = 8.0 \times 10^{-4}$. **g**, DFS analysis of patients with HCC, stratified by a median ratio of $CD3^{-}CD57^{+}$ NK counts relative to $DAPI^{+}$ cell counts at the IF (0.9028; NK^{high}: $n_{non\text{-}REC} = 21$, $n_{REC} = 10$; NK^{low}: $n_{non\text{-}REC} = 10$, $n_{REC} = 20$). The shaded areas correspond to 95% confidence intervals and the central lines indicate medians. Log-rank test: $P = 0.0066$. **h**, DSP images showing 64 regions of interest (white circles) from eight HCC tissues. **i**, Gene set enrichment of NK cell activation and differentiation in $CD57^{high}$ IF compartments. One-tailed permutation test. For statistical significance, $^{**}P < 0.01$ and $^{***}P < 0.001$. NES, normalized enrichment score. Full captions are available in the Supplementary Information.

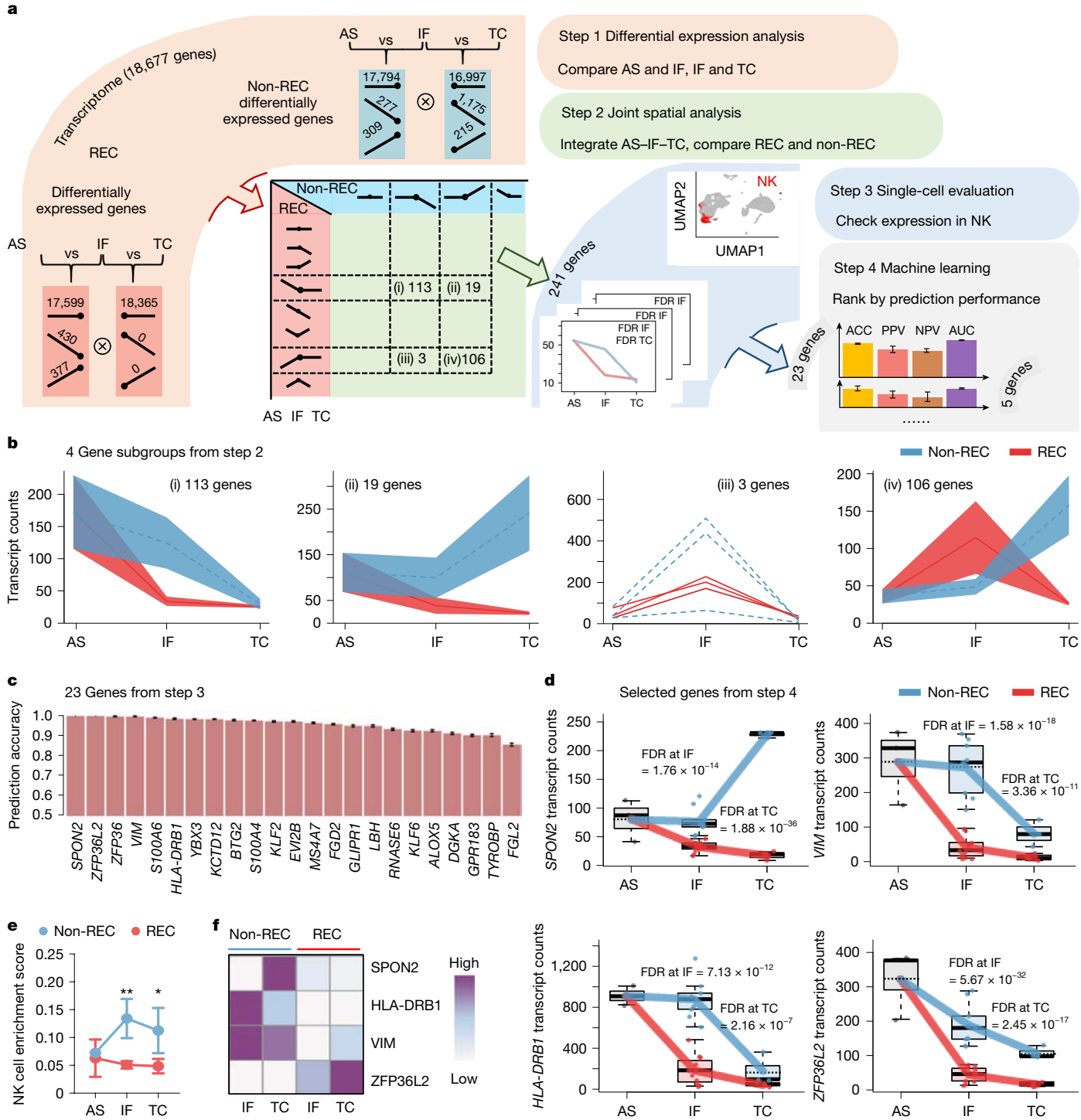

Fig. 2 | Identification of distinct spatial patterns of gene expressions for HCC recurrence prediction. a, Spatial transcriptomics analysis workflow: (1) differential expression analysis of 18,677 genes in NK cells across compartments, (2) identification of 241 spatially distinct genes, (3) filter for 23 genes that were differentially expressed in NK cells compared with other immune cells, and (4) test the predictive value of 23 genes for HCC recurrence using generalized linear models. ACC, accuracy; NPV, negative predictive value; PPV, positive predictive value. **b**, Gene expression patterns across the AS, IF and TC are distinctive between non-REC and REC HCC. The lines represent means, and the shaded areas show value spans. **c**, Model prediction accuracy for HCC recurrence (means ± s.d., $n = 100$ validation datasets). **d**, Spatial expression analysis of key genes. The boxplots show transcript counts with minima, maxima, median (centre line) and the first and third quartiles (box bounds). The whiskers extend to the most extreme data points not considered outliers (1.5× interquartile range). The lines connect compartment means. Two-sided Wald test with false discovery rate (FDR) control. **e**, Protein-based NK cell enrichment (means ± 2 s.e.m.). For sample sizes: AS (6 ROIs from 2 patients with non-REC versus 5 ROIs from 4 patients with REC), IF (9 ROIs from 2 patients with non-REC versus 21 ROIs from 4 patients with REC; $P = 0.0013$) and TC (6 ROIs from 2 patients with non-REC versus 14 ROIs from 4 patients with REC; $P = 0.038$). Unpaired two-tailed Student's t-test. **f**, Mean protein abundances of ROIs from two patients with non-REC and four patients with REC. For statistical significance, $^*P < 0.05$ and $^{**}P < 0.01$. Full captions are available in the Supplementary Information.

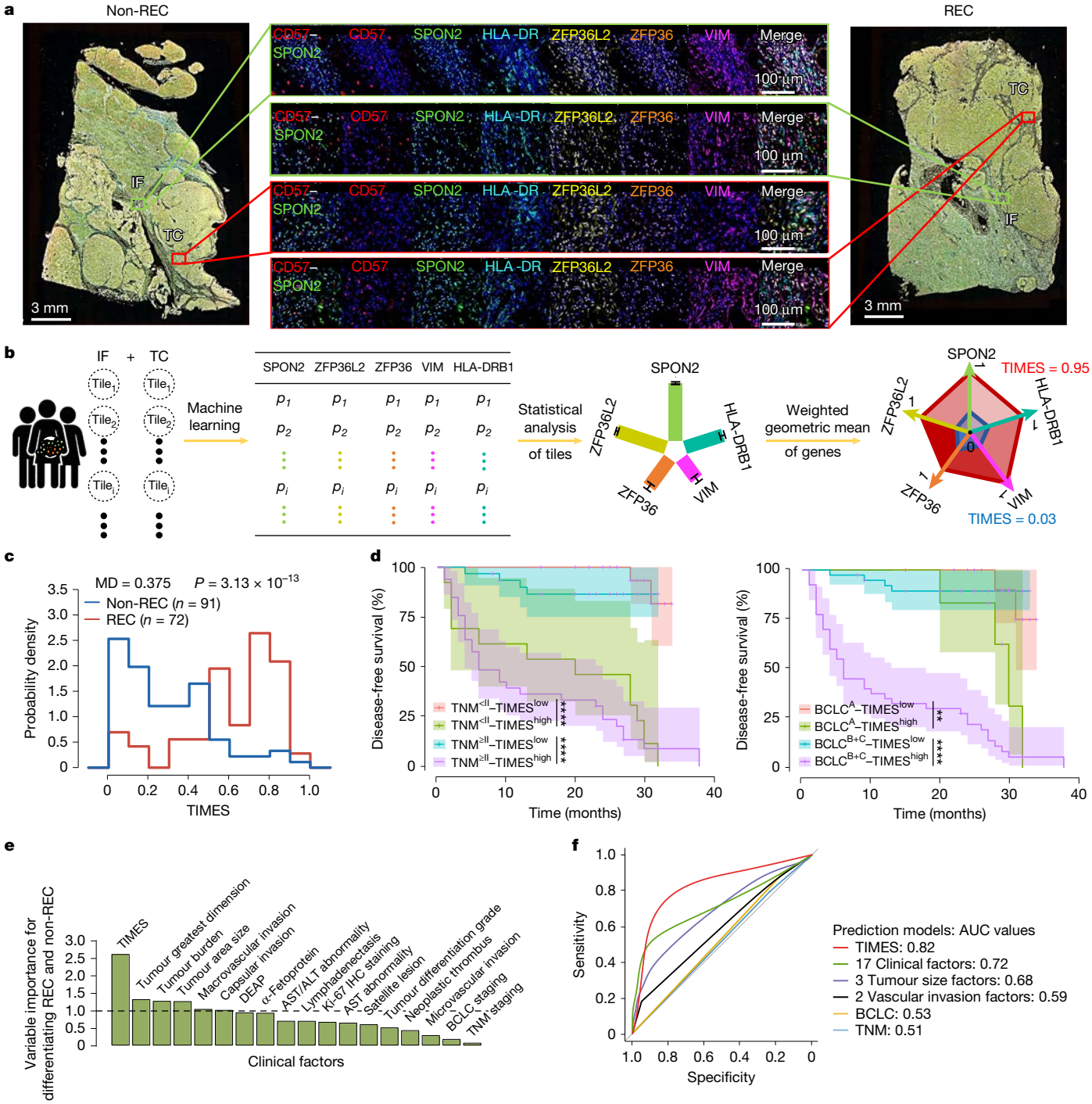

Fig. 3 | Development of a TIMES scoring system for HCC recurrence risk stratification. a, Representative mIHC images of non-REC and REC HCC tissues, showing nuclear staining (DAPI in blue) and biomarkers: CD57 (red), SPON2 (green), HLA-DR (cyan), ZFP36L2 (yellow), ZFP36 (orange) and VIM (magenta). **b**, TIMES scoring development using machine learning to integrate spatial and biomarker information. Model predictions are probability values (P_i), with final TIMES scores (0.03–0.95) presented as pentagons. **c**, TIMES score distributions for patients with REC ($n = 72$) and non-REC ($n = 91$) HCC. Unpaired two-tailed Wilcoxon rank-sum test ($P = 3.13 \times 10^{-13}$). MD, median difference of scores. **d**, DFS analysis combining TNM staging with TIMES scores (left) and BCLC with TIMES scores (right). The shaded areas correspond to 95% confidence intervals, and the central lines indicate medians. Log-rank test was used. For comparisons, $TNM^{<II}$–$TIMES^{low}$ ($n = 30$ patients) versus $TNM^{<II}$–$TIMES^{high}$ ($n = 23$ patients; $P = 3.0 \times 10^{-7}$), $TNM^{\geq II}$–$TIMES^{low}$ ($n = 50$ patients) versus $TNM^{\geq II}$–$TIMES^{high}$ ($n = 52$ patients; $P = 2.0 \times 10^{-8}$); $BCLC^{A}$–$TIMES^{low}$ ($n = 17$ patients) versus $BCLC^{A}$–$TIMES^{high}$ ($n = 9$ patients; $P = 0.01$), and $BCLC^{B+C}$–$TIMES^{low}$ ($n = 54$ patients) versus $BCLC^{B+C}$–$TIMES^{high}$ ($n = 50$ patients; $P = 1.0 \times 10^{-12}$). **e**, Variable importance from discriminant analysis, with values > 1 considered contributory (dashed line indicates variable importance = 1). ALT, alanine aminotransferase; AST, aspartate aminotransferase; DEAP, dynamic enhanced arterial phase. **f**, Receiver operating characteristic curves and AUC of TIMES, 17 factors (significant factors from univariate Cox regressions), 3-factor tumour size (tumour greatest dimension, area and burden), 2-factor vascular invasion (microvascular and macrovascular invasions), BCLC and TNM models. For statistical significance, $^{**}P < 0.01$ and $^{****}P < 0.0001$. Full captions are available in the Supplementary Information.

(1) the 17 significant clinical factors, (2) tumour size measurements, and (3) vascular invasion factors. The TIMES scoring system demonstrated significantly higher sensitivity and specificity (AUC = 0.82) than these models (Fig. 3f). In addition, the TIMES scoring system outperformed prediction models based solely on NK cell subsets, as demonstrated using a separate dataset of mIHC staining (Extended Data Fig. 3g). These findings highlight the superior prognostic value of the integrative approach of TIMES, which incorporates spatial information from the five biomarkers, compared with relying on any single clinical factor or biomarker (Extended Data Fig. 3h).

To explore the clinical utility of the TIMES scoring system in guiding personalized treatment strategies for patients with HCC, TIMES were applied by clinicians to stratify patients in a pilot cohort of 25 patients with HCC who received adjuvant anti-PD1 therapy after surgery (cohort 7; Supplementary Table 8). We observed that TIMES scores were higher in patients who partial responded to adjuvant anti-PD1 therapy than patients who were non-responders, with a median score difference of 0.267 ($P = 1.61 \times 10^{-3}$; Extended Data Fig. 3i and Supplementary Table 17). However, these preliminary findings require validation in larger cohorts. To facilitate access of TIMES in the clinical community, a web tool (https://sun.times.ustc.edu.cn/) was developed (Extended Data Fig. 4a, Supplementary Fig. 6a,b and Supplementary Video 1). By uploading standard pathological images of the HCC tissue from patients stained for the five biomarkers using commercially available antibodies, the web tool generates a report with TIMES score and recurrence risk; however, it is important to note that TIMES may warrant further investigation as a potential tool for stratifying patients in clinical trials of adjuvant immunotherapy for HCC (Extended Data Fig. 4b–d and Supplementary Fig. 7). Future studies shall explore how TIMES correlates with other established biomarkers and clinical outcomes in larger, prospective cohorts.

SPON2$^+$ NK: active and tumour infiltrating

To unravel the immunological underpinnings of the predictive power of TIMES, we investigated the functional roles of these biomarkers in shaping the TME. Of the five biomarkers, *SPON2* was the most predictive in our TIMES scoring system, leading us to explore its immunomodulatory effects and potential effect on HCC recurrence. Single-cell RNA-seq analysis of 18 patients with early-REC HCC[28] revealed that *SPON2* was particularly enriched in NK cells (Extended Data Fig. 5a,b). Compared with SPON2$^-$ NK cells, SPON2$^+$ NK cells expressed higher levels of activation markers (for example, *TNF*, *PRF1*, *IFNG*, *KLRC2*, *KLRK1*, *NCR3* and *NCR1*) and lower levels of inhibitory receptors (for example, *CD96*, *TIGIT*, *KLRC1*, *CTLA4* and *TGFB1*; Fig. 4a). Flow cytometric analysis of human peripheral blood further demonstrated that SPON2$^+$ NK cells expressed significantly higher levels of IFNγ ($P = 1.0 \times 10^{-4}$) and perforin ($P = 2.0 \times 10^{-4}$) than SPON2$^-$ NK cells (Fig. 4b). Similar results were found based on the single-cell RNA-seq dataset (Extended Data Fig. 5c). Gene Ontology analysis showed enrichment of pathways promoting antitumour NK cell function in SPON2$^+$ NK cells (Extended Data Fig. 5d). DSP transcriptomic data showed that SPON2^{high}CD57^{high} regions of interest (ROIs) had significantly higher expression of IFNγ receptor genes than SPON2^{low}CD57^{high} ROIs (Extended Data Fig. 5e). These findings demonstrate that *SPON2* expression delineates a highly activated and cytotoxic NK cell subset.

Given the spatial nature of the predictive value of TIMES, we next investigated the relationship between *SPON2* expression and the regional distribution of NK cells within the tumour. Visium spatial data revealed that SPON2$^+$ NK cells were enriched in the TC of non-REC tissues and the IF of REC tissues (Extended Data Fig. 5f). SPON2$^+$NK^{high} spots in the TC were enriched in pathways associated with immune activation, cell motility, leukocyte migration and leukocyte-mediated immunity (Extended Data Fig. 5g–i). Gene set enrichment analysis of DSP ROIs from the TC showed that SPON2^{high}CD57^{high} ROIs were enriched in pathways related to leukocyte chemotaxis, cell adhesion, innate immune response and immune responses to IFNγ, IL-12 and IL-18 (Extended Data Fig. 5j), indicating the migration potential of SPON2$^+$ NK cells. In a 3D-printed HCC tumour model (Fig. 4c), SPON2$^+$ NK92 cells exhibited enhanced migration towards HepG2 cells and increased IFNγ and perforin expression (Fig. 4d and Extended Data Fig. 6a–f). Overexpression of *SPON2* (NK92$^{OE\text{-}SPON2}$) promoted NK92 cell infiltration and IFNγ secretion, whereas *SPON2* knockdown (NK92$^{KD\text{-}SPON2}$) hindered migration (Fig. 4e–h, Extended Data Fig. 6g–i and Supplementary Videos 2–4). These findings suggest that SPON2 contributes to NK cell migration and cytotoxic activity against tumour cells.

SPON2$^+$ NK and CD8$^+$ T cell interactions

To investigate whether SPON2$^+$ NK cells interact with CD8$^+$ T cells in antitumour immune responses, we performed further analyses using mIHC and single-cell RNA-seq data. mIHC spatial mapping in 28 HCC tissues demonstrated that SPON2$^+$ NK cells are CD3$^-$CD68$^-$CD163$^-$CD16$^+$CD56$^+$CD57$^+$ (Extended Data Fig. 7a), confirming their identity as NK cells rather than T cells or macrophages. Ligand–receptor network analysis[38,39] of HCC single-cell RNA-seq data[28] revealed that the type II IFN (IFNγ) pathway was the primary immune-associated signal distinguishing SPON2$^+$ from SPON2$^-$ NK cells (Extended Data Fig. 7b,c), with CD8$^+$ T cells being predicted to be a major source of IFNγ acting on SPON2$^+$ NK cells (Extended Data Fig. 7d,e). mIHC spatial mapping of CD3, CD8, CD57, IFNγ and SPON2 in the WSI of 28 HCC tissues showed CD3$^+$CD8$^+$IFNγ$^+$ T cells in close proximity with CD3$^-$CD57$^+$SPON2$^+$ NK cells in the TC compartments (Fig. 4i and Supplementary Fig. 8). In non-REC tissues, the TC compartment had higher SPON2$^+$CD57$^+$ NK cell infiltration than the IF compartment ($P < 10^{-4}$), whereas in REC tissues, the IF compartment had higher infiltration ($P = 6.0 \times 10^{-4}$; Fig. 4j). CD8$^+$ T cells were more abundant proximal to SPON2$^+$CD57$^+$ NK cells than to SPON2$^-$CD57$^+$ NK cells ($P = 7.9 \times 10^{-3}$; Extended Data Fig. 8a–c). This spatial association indicates potential interactions between SPON2$^+$ NK cells and CD8$^+$ T cells, which may contribute to antitumour immunity.

To determine whether direct contact between CD8$^+$ T cells and SPON2$^+$ NK cells is required for CD8$^+$ T cell antitumoural activity, we performed co-culture experiments using HepG2 cells, *SPON2*-knockout (NK$^{KO\text{-}SPON2}$; Extended Data Fig. 8d,e) and *SPON2*-overexpression (NK$^{OE\text{-}SPON2}$) primary NK cells, and CD8$^+$ T cells. Transwell plates mimicked direct and indirect contact between NK$^{OE\text{-}SPON2}$ (or NK$^{KO\text{-}SPON2}$) and CD8$^+$ T cells. Direct co-culture of CD8$^+$ T and NK$^{OE\text{-}SPON2}$ cells induced significantly higher percentages of CD8$^+$ T cells expressing IFNγ ($P = 1.1 \times 10^{-3}$), TNF ($P = 5.4 \times 10^{-3}$), CD107a ($P = 7.6 \times 10^{-3}$) and granzyme B ($P = 1.0 \times 10^{-4}$) than co-culture with NK$^{KO\text{-}SPON2}$ cells (Fig. 4k,l and Extended Data Fig. 8f,g). Indirect co-culture resulted in decreased percentages of CD8$^+$ T cells expressing IFNγ and CD107a. Blocking IFNγ in the direct co-cultures significantly decreased the percentages of CD8$^+$ T cells expressing IFNγ ($P = 2.0 \times 10^{-2}$), TNF ($P = 2.1 \times 10^{-2}$) and CD107a ($P = 1.0 \times 10^{-2}$; Fig. 4l and Extended Data Fig. 8g). NK$^{OE\text{-}SPON2}$ cells showed higher cytotoxicity towards HepG2 cells than towards NK$^{KO\text{-}SPON2}$ cells in the direct co-culture (Extended Data Fig. 8h,i). Co-culturing HepG2 cells with both NK$^{OE\text{-}SPON2}$ (or NK$^{KO\text{-}SPON2}$) and CD8$^+$ T cells in a short-term (4-h) setting did not reveal a significant enhancement of CD8$^+$ T cell cytotoxic activity by NK$^{OE\text{-}SPON2}$ cells (Extended Data Fig. 8j,k and Supplementary Fig. 9a,b). These findings demonstrate that direct contact between SPON2$^+$ NK cells and CD8$^+$ T cells is necessary for their antitumoural activity, which is mediated by IFNγ signalling.

SPON2 loss in NK cells increases HCC recurrence

To elucidate the antitumour role of SPON2$^+$ NK cells in vivo, we used a set of HCC mouse models, including subcutaneous[40], orthotopic and

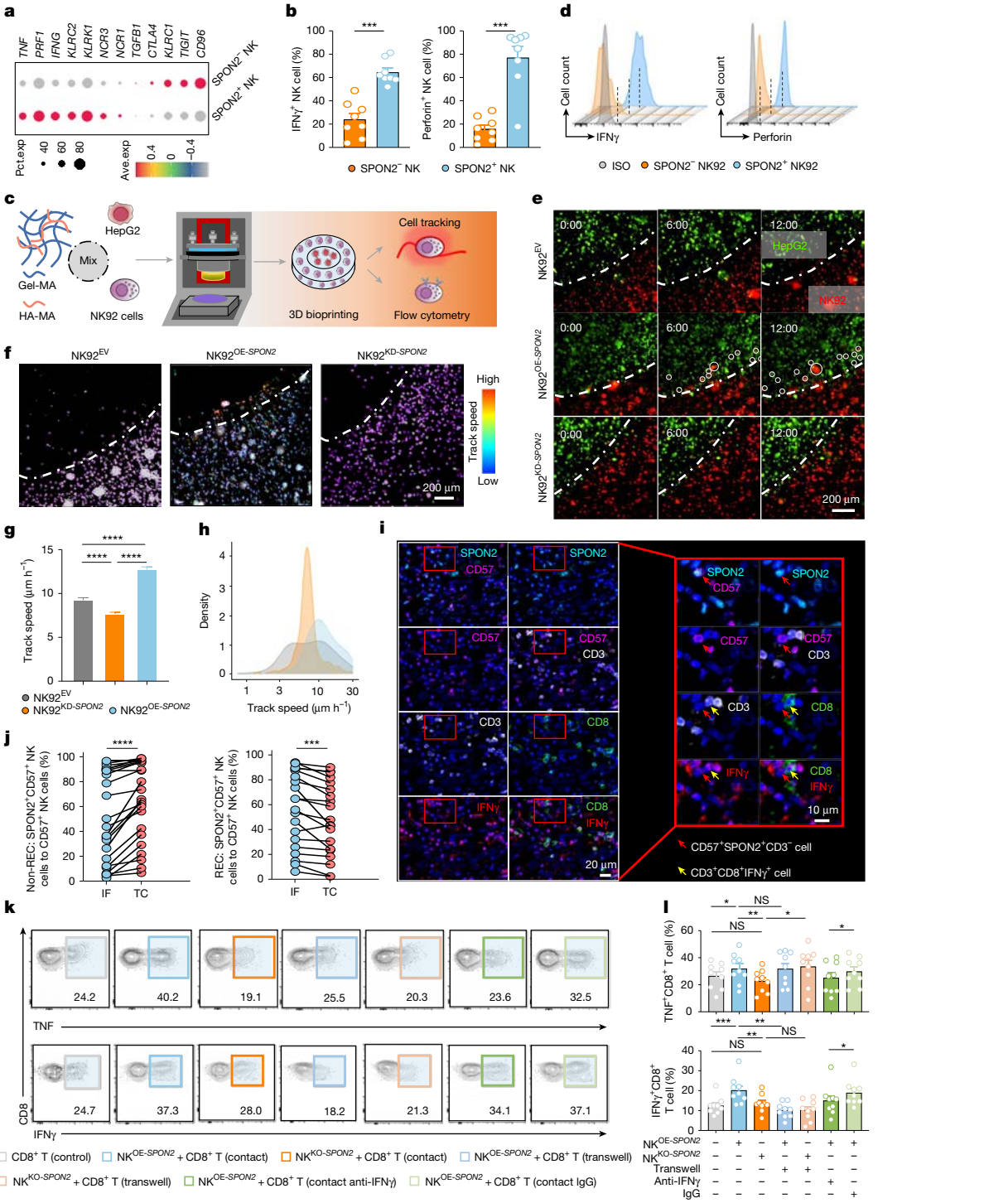

Fig. 4 | SPON2⁺ NK cells are activated with migration potential to the HCC TC and in proximity to higher abundance of IFNγ⁺CD8⁺ T cells. **a**, NK immunity-related marker expression in SPON2⁺ and SPON2⁻ NK cells. Ave. exp, average expression; Pct. exp, percentage expression. **b**, Flow cytometry of IFNγ⁺ and perforin⁺ NK proportions in SPON2⁻ versus SPON2⁺ NK cells ($n = 8$ patients per group). $P = 1.0 \times 10^{-4}$ and $P = 2.0 \times 10^{-4}$. **c**, 3D bioprinting schematic with HepG2 and NK92 cells. **d**, Flow cytometry of SPON2⁻ and SPON2⁺ NK92 cells after PMA/ionomycin stimulation. **e**, Migration tracking of empty vector NK92 cells ($NK92^{EV}$), $NK92^{OE\text{-}SPON2}$ and $NK92^{KD\text{-}SPON2}$ towards the HepG2 region. The white circles highlight NK92 cells that infiltrated to the tumour region. **f**–**h**, Migration analysis of NK92 cells with differential SPON2 expression. Representative trajectories (**f**), average track speed (**g**; $P < 1.0 \times 10^{-4}$), and track speed distribution (**h**) of $NK92^{EV}$ ($n = 491$ cells), $NK92^{KD\text{-}SPON2}$ ($n = 327$) and $NK92^{OE\text{-}SPON2}$ ($n = 464$) at the 12-h point. **i**, mIHC showing CD57⁺SPON2⁺CD3⁻ NK cells in proximity with CD3⁺CD8⁺IFNγ⁺ T cells. **j**, SPON2⁺CD57⁺ cell proportion comparison between the IF and the TC in patients with non-REC ($n = 23$; $P < 1.0 \times 10^{-4}$) and REC ($n = 20$; $P = 6.0 \times 10^{-4}$) HCC. **k**,**l**, Contact/transwell co-culture experiments comparing CD8⁺ T cell responses. Flow cytometry profiles (**k**) and quantification (**l**) of TNF and IFNγ expression in CD8⁺ T cells co-cultured with $NK^{OE\text{-}SPON2}$ or $NK^{KO\text{-}SPON2}$ cells, with or without IFNγ neutralization ($n = 9$ patients). Key comparisons for TNF⁺CD8⁺ T cells: $NK^{OE\text{-}SPON2}$ versus $NK^{KO\text{-}SPON2}$ contact ($P = 0.0054$), $NK^{OE\text{-}SPON2}$ contact versus transwell ($P = 0.98$), $NK^{OE\text{-}SPON2}$ + CD8⁺ T (contact anti-IFNγ) versus $NK^{OE\text{-}SPON2}$ + CD8⁺ T (contact IgG; $P = 0.021$); for IFNγ⁺CD8⁺ T cells: $NK^{OE\text{-}SPON2}$ versus $NK^{KO\text{-}SPON2}$ contact ($P = 0.0011$), $NK^{OE\text{-}SPON2}$ contact versus transwell ($P = 0.0011$), $NK^{OE\text{-}SPON2}$ + CD8⁺ T (contact anti-IFNγ) versus $NK^{OE\text{-}SPON2}$ + CD8⁺ T (contact IgG; $P = 0.02$). Unless otherwise specified, a paired two-tailed Student's *t*-test was used, and data are means ± s.e.m. For statistical significance, $^{*}P < 0.05$, $^{**}P < 0.01$, $^{***}P < 0.001$, $^{****}P < 0.0001$ and not significant (NS). Full captions are available in the Supplementary Information.

in situ transplantation recurrence models[41], using *Spon2*-knockout (*Spon2*$^{-/-}$) and wild-type (WT) mice (Fig. 5a,f and Extended Data Fig. 9a). Across all models, *Spon2*$^{-/-}$ mice consistently exhibited larger tumours, accelerated tumour growth, diminished immune cell infiltration and reduced percentages of IFNγ-producing NK and CD8$^+$ T cells, compared with WT mice (Fig. 5b–e,g,h and Extended Data Fig. 9b–h). These findings underscore the importance of *Spon2* in promoting the infiltration and effector functions of NK cells and CD8$^+$ T cells, thereby enhancing tumour control and reducing the risk of HCC recurrence.

To dissect the specific contribution of NK cells to the tumour-promoting effect of *Spon2* deficiency, we selectively depleted NK cells, CD8$^+$ T cells or both in HCC mouse models (Extended Data Fig. 9i). The significantly larger tumours observed in *Spon2*$^{-/-}$ mice than in WT mice were only evident when NK cells were present and CD8$^+$ T cells were depleted ($P < 10^{-4}$), but not upon NK cell depletion or combined depletion of both cell types (Extended Data Fig. 9j). To further validate the NK cell-dependent nature of this phenotype, we generated NK-specific *Spon2*$^{-/-}$ mouse models (Fig. 5i and Extended Data Fig. 9k,l). Conditional knockout of *Spon2* in NK cells (*Spon2*$^{f/f}$-*Ncr1*$^{Cre+}$) resulted in significantly larger tumours ($P = 7.8 \times 10^{-3}$; Fig. 5j and Extended Data Fig. 9m), reduced NK cell infiltration ($P = 8.0 \times 10^{-4}$) and decreased percentages of IFNγ-producing NK cells ($P = 3.4 \times 10^{-2}$) and CD8$^+$ T cells ($P = 1.0 \times 10^{-4}$; Extended Data Fig. 9n) compared with control mice (*Spon2*$^{f/f}$-*Ncr1*$^{Cre-}$). These findings conclusively demonstrate that the accelerated tumour progression observed in *Spon2*$^{-/-}$ mice is primarily driven by the loss of SPON2 function in NK cells.

The translational potential of SPON2$^+$ NK cells was further demonstrated by the adoptive transfer of human NK$^{OE\text{-}SPON2}$ cells, which led to significantly smaller human liver tumours than NK$^{KO\text{-}SPON2}$ cells in humanized HCC mice ($P = 3.9 \times 10^{-3}$; Fig. 5k,l and Extended Data Fig. 9o). Moreover, ex vivo-stimulated SPON2$^+$ NK cells (NK^{stimulated}) exhibited enhanced tumour suppression compared with unstimulated NK cells ($P = 1.4 \times 10^{-3}$; Extended Data Fig. 9p–s). Mass cytometry analysis of 43 specimens from 27 patients with HCC (cohort 4; Fig. 5m, Extended Data Fig. 10a and Supplementary Table 5) revealed high expression levels of SPON2 (48.9%; Fig. 5n and Extended Data Fig. 10b) and IFNγ (Extended Data Fig. 10c) in NK cells. Of note, SPON2$^+$ NK cell enrichment in the TC compartment was higher in patients with long DFS (2 years or longer; $P = 9.8 \times 10^{-3}$), whereas enrichment at IF was higher in patients with short DFS (less than 1 year; $P = 3.6 \times 10^{-3}$; Fig. 5o). SPON2$^+$ NK cell enrichment positively correlated with overall survival (Spearman's $\rho = 0.59$, $P = 0.034$; Extended Data Fig. 10d) and IFNγ$^+$ NK cell enrichment (Spearman's $\rho = 0.55$, $P = 1.6 \times 10^{-4}$; Extended Data Fig. 10e), highlighting the clinical relevance of SPON2$^+$ NK cells in HCC. Collectively, our in vivo studies using multiple HCC mouse models, coupled with the analysis of patient samples, provide evidence for the antitumour role of SPON2$^+$ NK cells in HCC (Extended Data Fig. 10f).

Discussion

In this study, we developed the TIMES scoring system based on the spatial expression patterns of five biomarkers (SPON2, ZFP36L2, ZFP36, VIM and HLA-DRB1) to predict HCC recurrence risk. Of note, the predictive power of these markers emerged only when their spatial context was considered, rather than focusing solely on expression levels of individual markers. Our validation studies in 231 patients from five multicentre cohorts suggest that TIMES scoring complements existing clinical factors and staging systems, particularly for early-stage HCC. Functional studies utilizing in vitro co-culture systems, 3D-printed tumour models and diverse mouse models (including NK cell-specific *Spon2*-knockout mice) revealed that SPON2 augments NK cell infiltration and increases IFNγ secretion, providing insights into the potential immunological underpinnings of the predictive capacity of TIMES.

Although traditional risk factors, tumour grading, staging and vascular invasion offer valuable prognostic information for patients with HCC, there remains room for improvement in predicting HCC recurrence, especially for early-stage HCC. Our study introduces TIMES as a potential tool to complement existing prognostic methods by integrating spatial immune information. In the analyses comparing TIMES against 118 clinical factors, including established predictors such as vascular invasion and tumour multiplicity[42,43], TIMES demonstrated significantly stronger associations with DFS ($P = 7.13 \times 10^{-10}$) and recurrence ($P = 1.52 \times 10^{-8}$). TIMES maintained its prognostic value for patients stratified by vascular invasion status, suggesting its potential to provide additional information beyond these established risk factors. Recognizing the heterogeneity of HCC aetiology, we stratified patients by hepatitis B virus and hepatitis C virus status, as well as the presence of liver fibrosis and cirrhosis (Supplementary Tables 18–21). TIMES showed consistent prognostic value across these subgroups, indicating potential applicability to diverse patient populations. However, we acknowledge that our current cohort is predominantly cirrhotic, and further validation in patients who are non-cirrhotic is necessary.

Although there are currently no standard adjuvant therapy protocols for patients with high-risk HCC supported by level I evidence, several ongoing phase III trials are investigating the efficacy of adjuvant immunotherapy in early-stage HCC[44,45]. Accurate risk stratification could facilitate patient selection for these trials and, potentially, guide future adjuvant therapy decisions. In a pilot cohort of patients receiving adjuvant anti-PD1 therapy, we observed that treatment responders had significantly higher TIMES scores than non-responders ($P = 1.61 \times 10^{-3}$). Although our initial results suggest that TIMES may have potential in predicting immunotherapy response, this finding is preliminary and has important limitations. Our pilot study had a small sample size and did not compare TIMES to established biomarkers such as PDL1 expression or tumour immune phenotype. Larger prospective studies are needed to rigorously evaluate TIMES against these and other predictive markers before any clinical utility can be determined. Our study focuses on patients with surgically resected HCC, which represents only a subset of the HCC population. We acknowledge that other treatment modalities, such as liver transplantation, ablation and embolization, have crucial roles in HCC management. Future studies should investigate the applicability of TIMES or similar immune-based prognostic markers in these diverse treatment settings.

The prognostic significance of tumour-infiltrating NK cells in HCC has been previously explored[9–20], but the precise spatial distribution of NK cells in patient tumours has not been extensively characterized[21]. Our mIHC analysis revealed insights into the prognostic value of different NK cell subsets. Of note, high CD3$^-$CD57$^+$ NK cell infiltration was associated with prolonged DFS, whereas CD3$^-$CD56$^+$ or CD3$^-$CD16$^+$CD56$^+$ NK cells did not show significant prognostic value. This finding suggests that mature NK cells (CD57$^+$) may have a special role in preventing HCC recurrence, possibly due to their enhanced cytotoxic capabilities.

Our functional studies suggest a potential role for SPON2$^+$ NK cells in HCC progression and recurrence. Through mIHC, mass cytometry and genetic models, we demonstrated the co-expression of SPON2 in NK cells within the HCC microenvironment. The development of *Spon2*$^{f/f}$-*Ncr1*$^{Cre+}$ mice provided evidence for a possible cell-autonomous role of SPON2 in NK cell-mediated tumour suppression, as these mice exhibited significantly larger tumours than control mice. The potential ways in which SPON2$^+$ NK cells control tumours appear to be multifaceted. Our investigation into the role of SPON2 in NK cell function using 3D-bioprinted tumour models provided valuable insights into its role in NK cell migration and antitumour activity. Using NK92$^{KD\text{-}SPON2}$ and NK92$^{OE\text{-}SPON2}$ cell lines, we demonstrated that SPON2 promoted NK cell motility and directional movement towards tumour cells. NK92$^{OE\text{-}SPON2}$ cells showed enhanced migration to HepG2-rich areas, covered larger areas and exhibited increased IFNγ secretion, compared with control cells. Conversely, NK92$^{KD\text{-}SPON2}$ cells displayed impaired directional

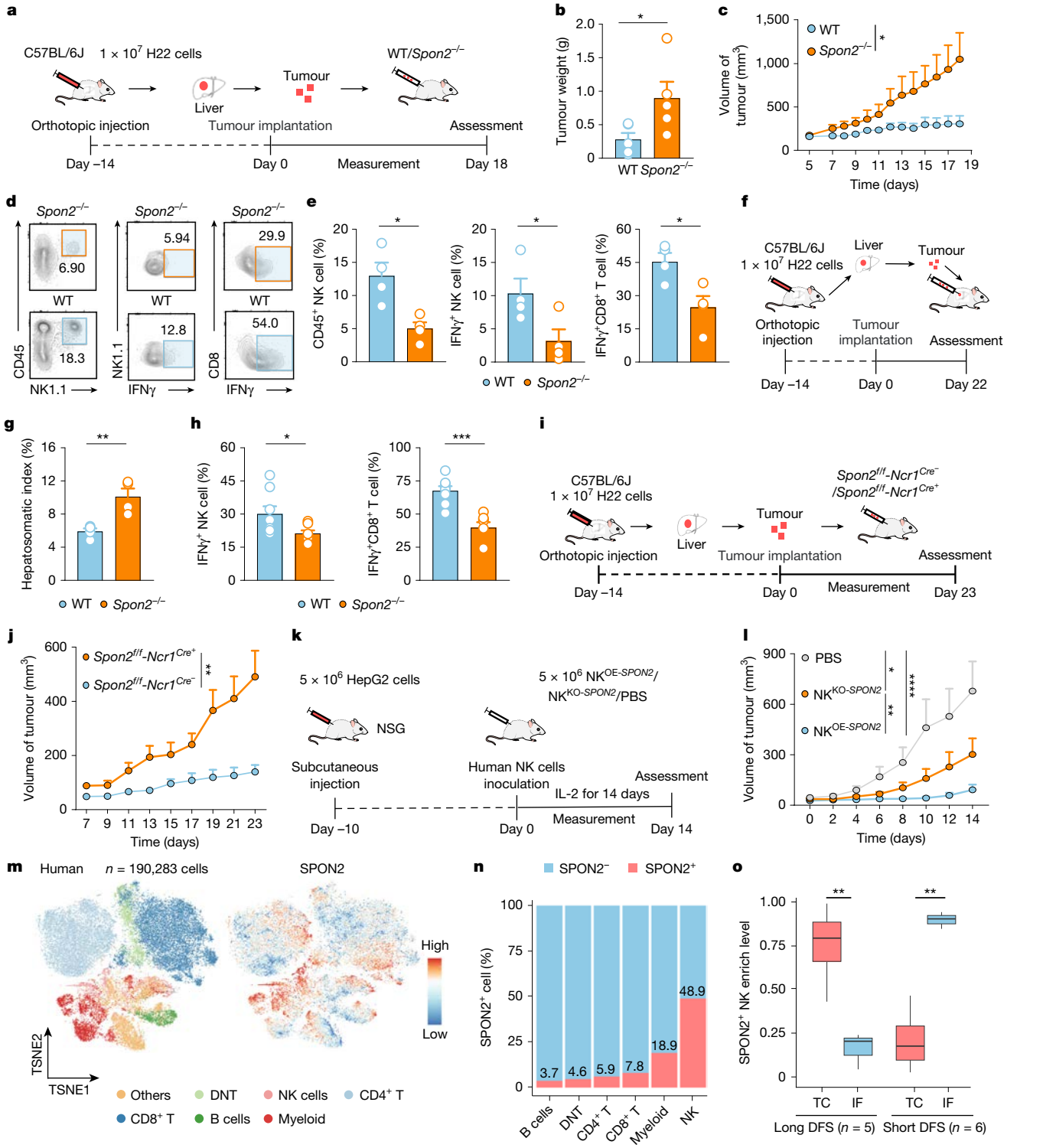

Fig. 5 | Effect of *Spon2* knockout on NK cell function in HCC mouse models. **a**–**c**, Subcutaneous HCC model. Experimental design (**a**), tumour weights (**b**; day 18, $P = 0.048$) and growth curves (**c**; $P = 0.048$). WT $n = 5$ versus *Spon2*$^{-/-}$ $n = 5$ mice. **d**,**e**, Flow cytometry analysis of tumour-infiltrating immune cells. Representative profiles (**d**) and quantification (**e**) of CD45$^+$ NK ($P = 0.012$), IFNγ$^+$ NK ($P = 0.048$) and IFNγ$^+$CD8$^+$ T ($P = 0.019$) cells. WT $n = 4$ versus *Spon2*$^{-/-}$ $n = 4$ mice. **f**–**h**, Orthotopic HCC model. Experimental design (**f**), hepatosomatic indices (**g**; day 22, WT $n = 4$ versus *Spon2*$^{-/-}$ $n = 4$ mice; $P = 0.0074$) and tumour-infiltrating IFNγ$^+$ NK and IFNγ$^+$CD8$^+$ T cells (**h**; WT $n = 8$ versus *Spon2*$^{-/-}$ $n = 7$ mice; $P = 0.046$ and $P = 2.0 \times 10^{-4}$). **i**,**j**, NK cell-specific *Spon2*-knockout model design (**i**) and tumour growth curves (**j**) comparing *Spon2*$^{f/f}$-*Ncr1*^{Cre} ($n = 5$) versus *Spon2*$^{f/f}$-*Ncr1*$^{Cre+}$ ($n = 5$) mice ($P = 0.0078$). **k**,**l**, HepG2 xenograft model with human NK cell transfer. Experimental design (**k**) and tumour growth curves (**l**) for PBS, NK$^{KO\text{-}SPON2}$ and NK$^{OE\text{-}SPON2}$ groups ($n = 5$ mice each; two-way analysis of variance: PBS versus NK$^{KO\text{-}SPON2}$, $P = 0.014$; PBS versus NK$^{OE\text{-}SPON2}$, $P < 1.0 \times 10^{-4}$; NK$^{OE\text{-}SPON2}$ versus NK$^{KO\text{-}SPON2}$, $P = 0.0039$). **m**–**o**, Mass cytometry analysis of tumour-infiltrating leukocytes. *t*-SNE projection and SPON2 expression (**m**), cell-type-specific SPON2$^+$ proportions (**n**) and SPON2$^+$ NK enrichment in patients with long (DFS ≥ 2 years, $n = 5$) and short (DFS < 1 year, $n = 6$) DFS (**o**). The boxplots show minima, median and maxima for long DFS at the TC (0.43, 0.80 and 1.00) versus the IF (0.04, 0.21 and 0.24), $P = 0.0098$; short DFS at the TC (0.03, 0.18 and 0.47) versus the IF (0.85, 0.91 and 0.95), $P = 0.0036$. DNT, double negative T cells. Unless otherwise specified, unpaired two-tailed Student's *t*-test was used and data are means ± s.e.m. For statistical significance, $^*P < 0.05$, $^{**}P < 0.01$, $^{***}P < 0.001$ and $^{****}P < 0.0001$. Full captions are available in the Supplementary Information.

movement and reduced migration distance. These findings align with the known functions of SPON2 in immune cell priming, recruitment and migration. Furthermore, $NK^{OE\text{-}SPON2}$ cells exhibited enhanced direct cytotoxicity against HepG2 cells and significantly increased $CD8^+$ T cell activation in co-culture conditions compared with $NK^{KO\text{-}SPON2}$ cells. This activation, indicated by elevated expression of IFNγ, TNF, CD107a and granzyme B, required direct cell-to-cell contact and was partially mediated by IFNγ. In a tri-culture model incorporating both immune cell types and tumour cells, we observed an even greater cytotoxic effect. These findings suggest a potential dual action for $SPON2^+$ NK cells: direct tumour cell killing and priming of adaptive antitumour immunity.

We acknowledge several limitations in our study. The development phase of the TIMES model relied on a relatively small discovery cohort from the DSP and LC–MS/MS analyses (Supplementary Table 22), which could potentially affect the initial identification of biomarkers. Although subsequent validation in 231 patients from five multicentre cohorts demonstrated the predictive power of these markers, mitigating initial sample size concerns, further validation in extensive cohorts is necessary. Larger-scale prospective studies should explore the applicability of TIMES across a broader spectrum of HCC presentations and treatment modalities. These studies should encompass diverse patient populations, including varied aetiologies of HCC and different ethnic backgrounds, to ensure the broad applicability of the TIMES scoring system. In addition, the attention to patients with early-stage, resectable HCC without previous treatment may limit the applicability of our results to other stages or treatment settings. Furthermore, our observations on NK cell migration and intercellular signalling mechanisms, particularly regarding interactions with $CD8^+$ T cells, are based on simplified experimental systems. Additional research using more complex models and functional assays is needed to fully elucidate these mechanisms and their implications for antitumour immunity in HCC. To facilitate the accessibility of TIMES to clinical community, we have developed a web tool (https://sun.times.ustc.edu.cn/) that can generate prognostic scores from routine IHC staining images. Although our results suggest potential applications for TIMES in HCC management, we emphasize that TIMES is currently a research-use-only tool. It has not been validated for clinical decision-making and should not be used to guide patient treatment at this stage. Further large-scale, prospective studies are needed to validate its clinical utility and safety before any consideration of its use in patient care. To assess the potential clinical acceptance of TIMES, we surveyed 203 oncologists across various specialties (Supplementary Tables 23 and 24). Although these survey results were encouraging and showed high interest in TIMES among clinicians, we acknowledge that stated preferences do not always translate directly to clinical practice. The actual implementation of TIMES will depend on further validation studies on real-world evidence of its effect on patient outcomes and regulatory approvals.

In conclusion, our study presents TIMES as a potential prognostic tool for HCC recurrence that integrates spatial immune information to enhance risk stratification beyond traditional clinical factors. The biological insights gained from our functional studies suggest avenues for future research into the role of $SPON2^+$ NK cells in HCC biology. As we move forwards with exploring the applicability of TIMES in other cancer types, this work lays the foundation for more personalized management strategies in early-stage HCC and potentially other solid tumours.

Online content

Any methods, additional references, Nature Portfolio reporting summaries, source data, extended data, supplementary information, acknowledgements, peer review information; details of author contributions and competing interests; and statements of data and code availability are available at https://doi.org/10.1038/s41586-025-08668-x.

1. Zhai, W. et al. The spatial organization of intra-tumour heterogeneity and evolutionary trajectories of metastases in hepatocellular carcinoma. *Nat. Commun.* **8**, 4565 (2017).
2. Rumgay, H. et al. Global burden of primary liver cancer in 2020 and predictions to 2040. *J. Hepatol.* **77**, 1598–1606 (2022).
3. Wu, J. et al. A noninvasive approach to evaluate tumor immune microenvironment and predict outcomes in hepatocellular carcinoma. *Phenomics* **3**, 549–564 (2023).
4. Brown, Z. J. et al. Management of hepatocellular carcinoma: a review. *JAMA Surgery* **158**, 410–420 (2023).
5. Singal, A. G., Kudo, M. & Bruix, J. Breakthroughs in hepatocellular carcinoma therapies. *Clin. Gastroenterol. Hepatol.* **21**, 2135–2149 (2023).
6. Elderkin, J. et al. Hepatocellular carcinoma: surveillance, diagnosis, evaluation and management. *Cancers* **15**, 5118 (2023).
7. Schürch, C. M. et al. Coordinated cellular neighborhoods orchestrate antitumoral immunity at the colorectal cancer invasive front. *Cell* **182**, 1341–1359.e19 (2020).
8. Casasent, A. K. et al. Multiclonal invasion in breast tumors identified by topographic single cell sequencing. *Cell* **172**, 205–217.e12 (2018).
9. Sun, C., Sun, H.-y, Xiao, W.-h, Zhang, C. & Tian, Z.-g Natural killer cell dysfunction in hepatocellular carcinoma and NK cell-based immunotherapy. *Acta Pharmacol. Sin.* **36**, 1191–1199 (2015).
10. Nersesian, S. et al. NK cell infiltration is associated with improved overall survival in solid cancers: a systematic review and meta-analysis. *Transl. Oncol.* **14**, 100930 (2021).
11. Lee, H. A. et al. Natural killer cell activity is a risk factor for the recurrence risk after curative treatment of hepatocellular carcinoma. *BMC Gastroenterol.* **21**, 258 (2021).
12. Juengpanich, S. et al. The role of natural killer cells in hepatocellular carcinoma development and treatment: a narrative review. *Transl. Oncol.* **12**, 1092–1107 (2019).
13. Xue, J. S. et al. The prognostic value of natural killer cells and their receptors/ligands in hepatocellular carcinoma: a systematic review and meta-analysis. *Front. Immunol.* **13**, 872353 (2022).
14. Zhao, J.-J. et al. Interleukin-37 mediates the antitumor activity in hepatocellular carcinoma: role for $CD57^+$ NK cells. *Sci. Rep.* **4**, 5177 (2014).
15. Chew, V. et al. Toll-like receptor 3 expressing tumor parenchyma and infiltrating natural killer cells in hepatocellular carcinoma patients. *J. Natl Cancer Inst.* **104**, 1796–1807 (2012).
16. Wu, Y. et al. Monocyte/macrophage-elicited natural killer cell dysfunction in hepatocellular carcinoma is mediated by CD48/2B4 interactions. *Hepatology* **57**, 1107–1116 (2013).
17. Sun, H. et al. Accumulation of tumor-infiltrating $CD49a^+$ NK cells correlates with poor prognosis for human hepatocellular carcinoma. *Cancer Immunol. Res.* **7**, 1535–1546 (2019).
18. Sun, H. et al. Human CD96 correlates to natural killer cell exhaustion and predicts the prognosis of human hepatocellular carcinoma. *Hepatology* **70**, 168–183 (2019).
19. Wu, M., Mei, F., Liu, W. & Jiang, J. Comprehensive characterization of tumor infiltrating natural killer cells and clinical significance in hepatocellular carcinoma based on gene expression profiles. *Biomed. Pharmacother.* **121**, 109637 (2020).
20. Pinyol, R. et al. Molecular predictors of prevention of recurrence in HCC with sorafenib as adjuvant treatment and prognostic factors in the phase 3 STORM trial. *Gut* **68**, 1065–1075 (2019).
21. Li, J. H. & O'Sullivan, T. E. Back to the future: spatiotemporal determinants of NK cell antitumor function. *Front. Immunol.* **12**, 816658 (2022).
22. Fu, T. et al. Spatial architecture of the immune microenvironment orchestrates tumor immunity and therapeutic response. *J. Hematol. Oncol.* **14**, 98 (2021).
23. Wu, L. et al. Spatially-resolved transcriptomics analyses of invasive fronts in solid tumors. Preprint at *bioRxiv* https://doi.org/10.1101/2021.10.21.465135 (2021).
24. Sorin, M. et al. Single-cell spatial landscapes of the lung tumour immune microenvironment. *Nature* **614**, 548–554 (2023).
25. Elhanani, O., Ben-Uri, R. & Keren, L. Spatial profiling technologies illuminate the tumor microenvironment. *Cancer Cell* **41**, 404–420 (2023).
26. Zhao, N. et al. Spatial maps of hepatocellular carcinoma transcriptomes highlight an unexplored landscape of heterogeneity and a novel gene signature for survival. *Cancer Cell Int.* **22**, 57 (2022).
27. Wu, R. et al. Comprehensive analysis of spatial architecture in primary liver cancer. *Sci. Adv.* **7**, eabg3750 (2021).
28. Sun, Y. et al. Single-cell landscape of the ecosystem in early-relapse hepatocellular carcinoma. *Cell* **184**, 404–421.e16 (2021).
29. Chang, J. et al. Genomic alterations driving precancerous to cancerous lesions in esophageal cancer development. *Cancer Cell* **41**, 2038–2050.e5 (2023).
30. Li, L. et al. Comprehensive proteogenomic characterization of early duodenal cancer reveals the carcinogenesis tracks of different subtypes. *Nat. Commun.* **14**, 1751 (2023).
31. Mund, A. et al. Deep Visual Proteomics defines single-cell identity and heterogeneity. *Nat. Biotechnol.* **40**, 1231–1240 (2022).
32. Xiang, H. et al. Region-resolved multi-omics of the mouse eye. *Cell Rep.* **42**, 112121 (2023).
33. Qu, Y. et al. A proteogenomic analysis of clear cell renal cell carcinoma in a Chinese population. *Nat. Commun.* **13**, 2052 (2022).
34. Cheung, C. C. L. et al. Residual SARS-CoV-2 viral antigens detected in GI and hepatic tissues from five recovered patients with COVID-19. *Gut* **71**, 226–229 (2022).
35. Kaya, N. A. et al. Multimodal molecular landscape of response to Y90-resin microsphere radioembolization followed by nivolumab for advanced hepatocellular carcinoma. *J. Immunother. Cancer* **11**, e007106 (2023).
36. Xu, X. F. et al. Risk factors, patterns, and outcomes of late recurrence after liver resection for hepatocellular carcinoma: a multicenter study from China. *JAMA Surg.* **154**, 209–217 (2019).
37. Lee, S. K. et al. Immunological markers, prognostic factors and challenges following curative treatments for hepatocellular carcinoma. *Int. J. Mol. Sci.* **22**, 10271 (2021).
38. Jin, S. et al. Inference and analysis of cell–cell communication using CellChat. *Nat. Commun.* **12**, 1088 (2021).
39. Medaglia, C. et al. Spatial reconstruction of immune niches by combining photoactivatable reporters and scRNA-seq. *Science* **358**, 1622–1626 (2017).

40. Predina, J. D. et al. Characterization of surgical models of postoperative tumor recurrence for preclinical adjuvant therapy assessment. *Am. J. Transl. Res.* **4**, 206–218 (2012).
41. Feng, Y. X. et al. Sorafenib suppresses postsurgical recurrence and metastasis of hepatocellular carcinoma in an orthotopic mouse model. *Hepatology* **53**, 483–492 (2011).
42. Lim, K. C. et al. Microvascular invasion is a better predictor of tumor recurrence and overall survival following surgical resection for hepatocellular carcinoma compared to the Milan criteria. *Ann. Surg.* **254**, 108–113 (2011).
43. Roayaie, S. et al. A system of classifying microvascular invasion to predict outcome after resection in patients with hepatocellular carcinoma. *Gastroenterology* **137**, 850–855 (2009).
44. Hack, S. P. et al. IMbrave 050: a phase III trial of atezolizumab plus bevacizumab in high-risk hepatocellular carcinoma after curative resection or ablation. *Future Oncol.* **16**, 975–989 (2020).
45. Bajorin, D. F. et al. Adjuvant nivolumab versus placebo in muscle-invasive urothelial carcinoma. *N. Engl. J. Med.* **384**, 2102–2114 (2021).

Publisher's note Springer Nature remains neutral with regard to jurisdictional claims in published maps and institutional affiliations.

Springer Nature or its licensor (e.g. a society or other partner) holds exclusive rights to this article under a publishing agreement with the author(s) or other rightsholder(s); author self-archiving of the accepted manuscript version of this article is solely governed by the terms of such publishing agreement and applicable law.

© The Author(s), under exclusive licence to Springer Nature Limited 2025

Methods

Patient sample collection

Tissue specimens were obtained from patients with primary HCC who underwent liver resection between 2018 and 2023, ensuring a continuous 5-year follow-up. This study includes a total of 278 clinical samples from seven cohorts (Supplementary Table 1):

(1) Cohort 1 encompassing 65 patients was obtained from the Department of Pathology, Anhui Provincial Hospital. Detailed clinical information of the included patients is listed in Supplementary Table 2.
(2) Cohort 2 encompassing 11 patients obtained from the Biobank of University of Science and Technology of China (USTC). Detailed clinical information of the included patients is listed in Supplementary Table 3.
(3) Cohort 3 encompassing 28 patients was obtained from Singapore General Hospital. Detailed clinical information of the included patients is listed in Supplementary Table 4, primarily containing gender, race, age, tumour size, TNM stage and histological grade information.
(4) Cohort 4 encompassing 27 patients was obtained from the Department of Hepatobiliary Surgery, the First Affiliated Hospital of USTC, and the involved samples were collected between 2018 and 2020 and were further examined through mass cytometry experiments. Detailed clinical information of the included patients is listed in Supplementary Table 5.
(5) Cohort 5 encompassing 128 patients were obtained from the Anhui Province Key Laboratory of Hepatopancreatobiliary Surgery, the First Affiliated Hospital of USTC, and the involved samples were collected from 2020 onwards. Detailed clinical information of the included patients is listed in Supplementary Table 6.
(6) Cohort 6 encompassing 19 patients was obtained from the Anhui Provincial Blood Center in China. Detailed clinical information of the included patients is listed in Supplementary Table 7.
(7) Cohort 7 encompassing 25 patients who underwent immunotherapy. Detailed clinical information of the included patients is listed in Supplementary Table 8.

A summary of the baseline characteristics from all the cohorts is provided in Supplementary Table 1, and multi-omics usage for the involved samples is presented in Supplementary Table 9. Ethical approval for this study was obtained from the Institutional Review Boards of Anhui Provincial Hospital in China (KY2021204 and KY2021212), the Biomedical Ethics Committee of University of Science and Technology of China (2019-N-(H)-121 and 2023-A-(H)-048), the Hunan Provincial Cancer Hospital Ethics Committee (JG2019-C485) and the Agency for Science, Technology and Research (A*STAR) in Singapore (IRB: 2021-161 and 2021-188).

Spatial transcriptomics sample preparation

Before sample preparation, all surfaces and work areas were decontaminated with RNaseZap RNase decontaminating solution. Formalin-fixed paraffin-embedded (FFPE) tissue was placed in an ice bath for 10–30 min before tissue sectioning using a microtome. Tissues were sectioned at a thickness of 5 μm and area of 6.5 × 6.5 mm^2 or less, for compatibility with Visium Spatial Gene Expression (10x Genomics) slides. The sections were floated on water (42 °C) for transfer to the capture area of the Visium spatial slide, ensuring that no air bubbles were trapped underneath; this process was repeated for the remaining three capture areas. The slides were initially dried for 3 h at 42 °C and then placed overnight at room temperature to complete the process. Subsequent deparaffinization, H&E staining, imaging and decrosslinking procedures were performed following the 10x Genomics user guide (CG000409, Rev A). The libraries were subsequently constructed according to the 10x Genomics user guide (CG000407, Rev A) and sequenced on the Illumina NovaSeq platform at a sequencing depth of approximately 40 million read pairs per spot.

Spatial transcriptomics data processing and visualization

Space Ranger (v1.3.1) was used to process the raw fastq files. The raw sequencing reads were aligned to the human reference genome (GRCH38). Seurat (v4.0.5) was used for processing the Space Ranger output files. FindIntegrationAnchors were used to integrate samples from 17 patients, an SCT model matrix named 'Integrated' with 76,599 spots (containing 3,000 characteristic genes) was generated. This matrix was then used to perform principal component analysis and UMAP clustering. The Integrated matrix takes integrated samples into account, including the connections between them, aiming to remove systematic biases while preserving biological variation. After data normalization using SCTransform, RunPCA was applied for dimension reduction, and the ST spots were clustered using FindNeighbors and FindClusters. As each spot contained more than one cell type, the AddModuleScore function was subsequently used to predict the main cell types. FindALLMarkers identified DEGs in each cluster. The functional parameters were set to 'threshold = 0.25, min.pct = 0.1'. Metascape[46] was used for Gene Ontology enrichment analysis. For data visualization, the following R packages were utilized: data.table (v1.14.2), RColorBrewer (v1.1-3), dplyr (v1.0.7), cowplot (v1.1.1), hdf5r (v1.3.5), ggplot2 (v3.3.5), viridis (v0.6.4), gpubr (v0.4.0), ggridges (v0.5.4), tidyverse (v1.3.1), colorspace (v2.0-2), readxl (v1.4.3), showtext (v0.9-4) and igraph (v1.2.7).

Immunohistochemistry

IHC was performed on 4-μm-thick FFPE tissue sections using the BenchMark ULTRA IHC/ISH System (Roche), in which tissue sections were subjected to deparaffinization, epitope retrieval, incubation with primary antibody and an enzymatic deposition of the brown chromogen 3,3′-diaminobenzidine (DAB). WSIs were then obtained via scanning of the IHC slides in the Axioscan Z7 Microscope Slide Scanner (Zeiss). Antibodies used for staining include glypican 3, CD34 and glutamine synthetase. Information on the antibodies used in the panel setup is provided in Supplementary Table 25.

Reticulin staining

The reticulin stain kit (Bio-Channel) was used for fibre dyeing. After the tissue was dehydrated, it was then oxidized with Gomori oxidant, bleached with an oxalic acid solution, washed with a ferric ammonium sulfate solution, stained with Gomori silver ammonia solution, and finally reduced with Gomori reducing agent. Each step required rinsing with running water for 5 min. After dehydration and transparency, the WSIs were then obtained by scanning with the Axioscan Z7 Microscope Slide Scanner (Zeiss).

Definition of immune cell gene sets

To delineate distinct levels of lymphocyte leukocyte infiltration in the Visium spatial slides, we established immune cell phenotypes using respective immune cell-related gene sets as follows[47,48]. T cells: *CD3D*, *CD3E*, *CD4*, *CD8A*, *CD8B*, *GZMA* and *CTLA4*; B cells: *CD19*, *CD79A*, *CD79B* and *CD27*; NK cells: *NCAM1*, B3GAT1, *NCR1*, *CD226*, *LAMP1*, *GNLY*, *KLRD1*, *CD69*, *CD7*, *NKG7* and *CXCR6*; myeloid cells: *ITGAX*, *ITGAM*, *CD68*, *MRC1*, *CD163*, *CD14*, *CLEC9A*, *BCL11A*, *CD86*, *NOS2*, *IRF5* and *VCAN*. The average expression level of the gene set can be quantified by an enrichment score, reflecting the abundance of each immune cell type. The score was calculated using the AddModuleScore function in Seurat, as previously described, with function parameters 'ctrl = 5, nbin = 10'.

Gene set enrichment analysis

To determine significantly over-represented or down-represented gene sets between two to-be-compared groups, we used GSEA[49,50] (v4.2.3), a computational tool. As summarized in Fig. 1i, we identified the genes that were expressed differently between nine ROIs from two patients with non-REC and four ROIs from two patients with REC. The genes

were ranked based on the $\log_2$ fold changes of expression, with the most substantial positive $\log_2$ fold changes on the left of the *x* axis, indicating high expression in HCC non-REC samples, and the most substantial negative $\log_2$ fold changes on the right of the *x* axis, indicating high expression in HCC REC samples. Subsequently, we computed an enrichment score for a specific gene set by traversing the list of $\log_2$ fold changes. The running-sum statistic increased with each encounter of a gene in the positive regulation of NK cell activation gene set (upper panel) or NK cell differentiation gene set (lower panel), and decreased for genes not belonging to the set. The magnitude of the increase or decrease was determined by the $\log_2$ fold change. The final enrichment score was where the running-sum statistic showed the largest deviation from zero. After normalizing the final enrichment score for the respective gene set size, we obtained the normalized enrichment score (NES) and determined its statistical significance through permutation tests.

Similarly, as shown in Extended Data Fig. 5i, we identified the genes that are expressed differently between $SPON2^+NK^{high}$ spots and $SPON2^+NK^{low}$ spots. These genes were ranked based on the $\log_2$ fold changes of expression, with the most substantial positive $\log_2$ fold changes on the left of the *x* axis, indicating high expression in $SPON2^+NK^{high}$ samples, and the most substantial negative $\log_2$ fold changes on the right of the *x* axis, indicating high expression in $SPON2^+NK^{low}$ samples. Subsequently, we computed an enrichment score for a specific gene set by traversing the list of $\log_2$ fold changes. The running-sum statistic increased with each encounter of a gene in the positive regulation of leukocyte migration gene set (upper panel) or leukocyte-mediated immunity gene set (lower panel), and decreased for genes not belonging to the set. We determined the magnitude of the increase or decrease, the final enrichment score, the NES as well as its statistical significance in the same way as described above.

Multiplex immunohistochemistry

mIHC was conducted on FFPE tissue sections using the Bond Max autostainer (Leica Biosystems) following established protocols[51–54]. The tissue sections were then subjected to deparaffinization, followed by repeated cycles of heat-induced epitope retrieval, endogenous peroxidase blocking (Leica Biosystems), incubation with primary antibodies (see Supplementary Table 25 for antibody details), secondary antibodies (Bond Refine Kit, Leica Biosystems) and Opal tyramide signal amplification (TSA; Akoya Biosciences). Finally, spectral DAPI (Akoya Biosciences) was applied as the nuclear counterstain.

The slides were then mounted in ProLong Diamond Anti-Fade Mountant (Molecular Probes, Life Technologies), and incubated in the dark at room temperature for 24 h. WSIs for each patient were captured using a PhenoImager HT Instrument Automated Quantitative Pathology Imaging System (Akoya Biosciences), visualized using a Phenochart Whole-Slide Viewer (Akoya Biosciences), and subsequently analysed and quantified using InForm software (v2.6.0; Akoya Biosciences) and HALO (v3.6; Indica Labs). The whole tissue was annotated by pathologists (Y.Z. and J.Y. from Singapore General Hospital) into three tissue compartments (AS, IF and TC). For each WSI, it comprised 100–600 tiles depending on the size of the tissue, and each tile measured 924 μm × 692 μm. The individual tiles were subsequently analysed and quantified using InForm (v2.6.0; Akoya Biosciences), QuPath (v0.4.0)[55] and HALO software[34,35]. The analysis involved the tiles being segmented at the single-cell level using an in-built pre-trained deep learning-based algorithm in HALO. Thereafter, the cell-type annotations and quantifications based on the expression of specific markers were conducted by trained pathologists (Y.Z. and J.Y. from Singapore General Hospital). CD57 was included due to its greater specificity[56–58] and superior prognostic value in HCC[13]. NK cells were identified as $CD3^-CD56^+$ ordinary NK, $CD3^-CD16^+CD56^+$ cytotoxic NK and $CD3^-CD57^+$ mature NK cells populations.

Separately, PhenoCycler analysis (Extended Data Fig. 8b,c) was done as described in the following. A PhenoCycler (Akoya Biosciences) was used to analyse FFPE tissues according to the manufacturer's instructions. In brief, tissue sections (thickness of 4 μm) were affixed to poly-L-lysine-coated coverslips, followed by deparaffinization and rehydration. Tissue retrieval was performed according to the method described[7,59,60]. Subsequently, the tissues underwent fixation for 20 min using prestaining fixing solution, followed by washing with tissue hydration buffer. An antibody cocktail, encompassing antibodies specific for CD3, CD8, CD57, IFNγ and SPON2, was applied to the coverslip, and staining was performed in a sealed humidity chamber for 3 h. Post-staining, the coverslips underwent a 4-min wash with staining buffer and were fixed in wells containing 1.6% paraformaldehyde for 10 min. This was succeeded by three washes in PBS (3 min per wash). The coverslips were then incubated in 100% methanol on ice for 10 min, followed by three washes in PBS. Fresh fixative solution was prepared immediately before the final fixation, which was performed at room temperature for 20 min, followed by three washes in PBS. Next, a PhenoCycler reporter plate containing the reporter master mix was prepared for every cycle. The PhenoCycler multicycle reaction and subsequent image acquisition were executed using an Akoya PhenoCycler instrument equipped with a 20× long working distance objective (NA of 0.7, FN of 22). Throughout imaging, the tissue was maintained in H2 buffer. Hybridization of the fluorescent oligonucleotides was performed in rendering buffer. After imaging, the fluorescent oligonucleotides were removed using stripping buffer. Data processing and analysis were performed using the PhenoCycler Analysis Manager and PhenoCycler Multiplex Analysis Manager of the individual tiles and were subsequently analysed and quantified using QuPath (v0.4.0)[55] and HALO software[34,35]. The analysis involved the tiles being segmented at the single-cell level using an in-built pre-trained deep learning-based algorithm in HALO. Thereafter, the cell-type annotations and quantifications based on the expression of specific markers were conducted by trained pathologists (Y.Z. and J.Y. from Singapore General Hospital).

DSP analysis

To further investigate the role of $CD3^-CD57^+$ NK, we used the GeoMx DSP Human Whole Transcriptome Atlas to assess 18,677 protein-coding human genes in 64 ROIs from eight HCC tissues (cohort 1). For quartile 3 normalization, individual counts were normalized against the 75th percentile of the signal from their respective ROIs[61]. We scaled the ROIs to the same value for their quartile 3 value by first dividing all genes per ROI by their corresponding quartile 3 count and then multiplying all genes in all ROIs by a constant, defined as the geometric mean of quartile 3 counts for all ROIs. This approach is commonly effective for cancer transcriptome assay and whole-transcriptome assay data and is often the preferred normalization method. The ceiling function was used to round the data after quartile 3 normalization. DESeq2 (v1.32.0) was used for differential gene expression analysis between different groups. Gene set enrichment analysis was performed as described earlier. Gene Set Variation Analysis (v1.44) was used to reveal the expression patterns of different gene sets and clarify the regulatory mechanisms and signalling pathways involved in these biological processes.

Identification of distinct spatial patterns of gene expressions for HCC recurrence prediction

We used deep spatial transcriptome sequencing to measure a total of 18,677 genes across NK-enriched ROIs in the AS, IF and TC compartments of tissues from four patients with non-REC and four patients with REC. The analysis flow consisted of four major steps (Fig. 2a).

Step 1: differential expression analysis. In REC HCC, 807 DEGs (determined at a false discovery rate of 2.5×10^{-3} in consideration of multiple testing, including 430 downregulated and 377 upregulated genes) were identified in the comparison between the AS and the IF, whereas no DEGs were identified between the IF and the TC. In non-REC HCC, 586 DEGs (277 downregulated and 309 upregulated) were identified by

comparing the AS to the IF, whereas 1,390 DEGs (1,175 downregulated and 215 upregulated) were identified by comparing the IF to the TC (Supplementary Table 10).

Step 2: joint spatial analysis. To further characterize the spatial expression patterns of the identified DEGs, we performed a joint spatial analysis to examine expressions across the AS, IF and TC compartments of non-REC that appeared distinct from those of REC HCC. Increased or decreased gene expression from one compartment to the adjacent compartment was marked as uptrend ('up') or downtrend ('down') lines, respectively, whereas no change was marked as flat ('flat') lines. Such analysis identified a total of 241 DEGs that can be categorized into four subgroups based on their spatial expression patterns from AS to IF to TC (Fig. 2b): (1) 113 DEGs exhibited a 'down-flat' pattern in REC tissues and a 'flat-down' pattern in non-REC tissues; (2) 19 DEGs showed a 'down-flat' pattern in REC tissues and a 'flat-up' pattern in non-REC tissues; (3) three genes had an 'up-flat' pattern in REC tissues and a 'flat-down' pattern in non-REC tissues; and (4) 106 genes displayed an 'up-flat' pattern in REC tissues and a 'flat-up' pattern in non-REC tissues (Supplementary Table 11).

Step 3: single-cell evaluation. The 241 DEGs were subject to an NK cell ligand–receptor analysis based on independent single-cell RNA sequencing data (HCC dataset previously reported[28]) using CellChat and NicheNet tools, finding that 23 DEGs were differentially expressed in NK cells compared with other immune cells.

Step 4: machine learning. We evaluated the predictive capability of the identified 23 DEGs for HCC REC outcomes using machine learning models. Specifically, we constructed generalized linear models (GLMs) for individual genes based on the transcript reads from ROIs in the IF and TC compartments. We fitted the gene-specific and compartment-specific transcript reads pertaining to patients with REC or non-REC HCC to negative binomial distributions. On the basis of these distributions, we randomly generated 1,000 recurrent case samples and 1,000 non-REC control samples using the bootstrapping technique. We then divided these case and control samples into a training set of 750 cases and 750 controls, and a validation set of 250 cases and 250 controls. The model was trained on the training dataset, and its performance was evaluated on the validation dataset using multiple performance indices including prediction accuracy (defined as the number of correctly classified samples compared with the total number of trials), positive predictive value, negative predictive value and the AUC. To estimate confidence intervals for these performance indices, we repeated this training and validation process 100 times (model performance results are presented in Fig. 2c, Supplementary Table 12 and Supplementary Fig. 3). Five genes (*SPON2*, *ZFP36L2*, *ZFP36*, *VIM* and *HLA-DRB1*) demonstrated superior performance.

In addition, we explored the predictive capability of two-gene combinations out of the five genes. For this purpose, we selected *SPON2*, as its GLM exhibited the best performance among all genes, and paired it with other genes (*SPON2* and *ZFP36L2*, *SPON2* and *ZFP36*, *SPON2* and *VIM*, and *SPON2* and *HLA-DRB1*). Using similar GLMs, we included compartment-specific transcript reads as predictor variables in the combination models: *SPON2* transcript reads at IF and TC, and the transcript reads of another gene at IF and TC (Supplementary Fig. 3).

LC–MS/MS preparation

FFPE tissue samples were processed using standard procedures[30,33], and 15 serial tissue sections (thickness of 5 μm) were prepared from each sample. These sections were placed at 65 °C for 1.5 h, cooled to room temperature and then deparaffinized by immersion twice in xylene (15 min each). Subsequently, the sections were dehydrated in a graded alcohol series (100%, 95%, 85%, 75% and pure water; 5 min each) and air-dried.

We applied a previously reported microbiopsy method for sampling from each FFPE sample[29,31,32,62]. The subsequent protein extraction, LC–MS/MS analysis, and qualitative and quantitative assessments of proteins were performed using established methods[30]. We applied laser capture microdissection to precisely dissect the sections of the samples[63]. Microdissection was performed using a Leica LMD 6500 laser microdissection system. According to the WHO classification, all samples were systematically evaluated by more than two expert pathologists to confirm the histopathological diagnosis and variant histology. Subtype samples were collected in 1.5-ml tubes and stored at −80 °C until further processing.

All samples were microdissected, collected in 1.5-ml EP tubes, and stored at −80 °C. Protein extraction was performed using TCEP. The method of TCEP extraction protein was applied in this study[64]. Specifically, 50 μl of TCEP buffer (containing 2% sodium deoxycholate, 40 mM 2-chloroacetamide, 100 mM Tris(2-carboxyethyl) phosphine hydrochloride, 10 mM (2-carboxyl)-phosphine hydrochloride and 1 mM phenylmethylsulfonyl fluoride in MS water, pH 8.5) was added to the samples, followed by heating in a 99 °C metal bath for 30 min. After cooling to room temperature, 3 μg of trypsin (reference: V528A, Promega) was added, and the mixture was incubated at 37 °C for 18 h.

Next, 13 μl of 10% formic acid was added, vortexed for 3 min and centrifuged at 12,000*g* for 5 min. The supernatant was collected into a new 1.5-ml tube with 350 μl of extraction buffer (0.1% formic acid in 50% acetonitrile), vortexed for 3 min and centrifuged again. The supernatant was transferred to a new tube and dried in a vacuum drier at 60 °C.

To dissolve the peptides, 100 μl of 0.1% formic acid was added, vortexed for 3 min and centrifuged for 3 min at 12,000*g*. The supernatant was desalinated using activated 3 M C18 disks. The activation included rinsing with 90 μl of 100% acetonitrile twice, followed by 90 μl of 50% and 80% acetonitrile once each, and then another rinse with 90 μl of 50% acetonitrile. After balancing the disks with 90 μl of 0.1% formic acid twice, the supernatant was loaded onto the disks twice and washed with 90 μl of 0.1% formic acid twice. Finally, 90 μl of elution buffer (0.1% formic acid in 50% acetonitrile) was added for elution, and the effluent was collected for MS analysis. The lipid extract was then dried in a vacuum drier at 60 °C.

Proteome analysis in LC–MS/MS analysis

For proteomic profiling, peptides were analysed using a Q-Exactive HFX Hybrid Quadrupole-Orbitrap Mass Spectrometer (Thermo Fisher Scientific) coupled with an EASY nLC 1200 HPLC system. Dried peptide samples were redissolved in solvent A (0.1% FA in water) and loaded onto a 2-cm self-packed trap column (100 μm ID, 3 μm ReproSil-Pur C18-AQ beads). They were then separated on a 150-μm ID column (15 cm in length, 1.9 μm ReproSil-Pur C18-AQ beads) over a 150-min gradient at a flow rate of 600 nl min^{-1} (solvent A: 0.1% FA in water; solvent B: 0.1% FA in 80% ACN).

Eluted peptides were ionized at 2.0 kV and introduced into the mass spectrometer in data-dependent acquisition mode. MS1 spectra were acquired in the *m*/*z* range of 300–1,400 at a resolution of 120,000, with an automatic gain control target of 3×10^6 and a maximum ion injection time of 80 ms. MS2 spectra were obtained in ion trap mode, fragmenting precursor ions using higher-energy collision dissociation at 27% normalized collision energy. Fragment ions were analysed with an automatic gain control target of 5×10^4 and a maximum ion injection time of 20 ms. Peptides triggering MS/MS scans were dynamically excluded for 12 s. Samples were randomly assigned numbers for proteomic analysis.

Quantification of global proteomic data and analysis

In our study, all MS raw files were processed using the Firmiana platform (https://phenomics.fudan.edu.cn/firmiana/gardener/). Trypsin was the proteolytic enzyme, allowing for up to two missed cleavages. Carbamidomethyl (C) was designated as a fixed modification, whereas

variable modifications included oxidation (M) and acetylation (protein N terminus) for proteome data. Peptides were quantified on the Firmiana platform based on MS1 intensity peak areas. Mass tolerances were set at 20 ppm for precursors and 50 mmu for products. Precursor ion charge states were limited to +2, +3 and +4, with false discovery rates for peptide-spectrum matches and proteins capped at 1%. Label-free protein quantification was performed using the iBAQ algorithm, which calculated protein abundance by dividing the intensity of identification peptides by the number of theoretically observable peptides[65]. The FOT, defined as the iBAQ of a protein divided by the total iBAQ of all identified proteins in a sample, represented the normalized abundance of specific proteins across samples. Finally, TIMER2.0 (ref. 66) was used to estimate immune infiltration in the ROI. The R software package DEP (v1.20.0) was used for differential protein expression analysis and principal component analysis.

Development of the TIMES scoring system

In the mIHC staining analysis, we meticulously selected an average of five representative tiles from both the IF and the TC compartments of tissues obtained from 231 patients with HCC from cohorts 1, 2, 3, 5 and 7 (Fig. 3a and Supplementary Tables 2–4, 6 and 8). The proportion values of cells labelled for each of the five identified biomarkers with predictive potential ($SPON2^+$, $ZFP36L2^+$, $ZFP36^+$, VIM^+ or $HLA\text{-}DRB1^+$) were determined in these tiles.

First, to determine the best-performing machine learning algorithm based on these single-biomarker-labelled cell proportion values across the IF and TC compartments, we used mIHC data of 61 patients with HCC from cohort 1 (Supplementary Table 2). This dataset included cell proportion values for 148 tiles from the IF compartment and 148 tiles from the TC compartment of 31 non-REC tissues, and for 145 tiles from the IF compartment and 145 tiles from the TC compartments of 30 REC tissues. Using these cell proportion values as predictor variables in predicting HCC recurrence, we tested a battery of machine learning algorithms, including GLMs, support vector machines with a linear or radial kernel, decision tree models, random forest models and extreme gradient boosting models. To prepare effective input samples for modelling, we exhausted all the possible combinations of tile-specific single-biomarker-labelled proportion values in the IF and TC compartments of tissues from the same patient. Ultimately, 734 and 687 effective samples were obtained from non-REC and REC tissues, respectively. We randomly selected 75% of the samples for model training (tile measurements from 46 patients) and reserved the remaining 25% for validation (tile measurements from 15 patients). The training-validation process was repeated 100 times to estimate confidence intervals for the key performance indicators prediction accuracy, positive predictive value, negative predictive value and AUC based on the validation data (see Supplementary Table 13 for a model performance summary). We found that the extreme gradient boosting models provided the best overall performance, yielding HCC recurrence prediction accuracies of 89.8% based on SPON2-labelled data, and more than 85% based on ZFP36L2-labelled, ZFP36-labelled, VIM-labelled or HLA-DRB1-labelled data. When SPON2 was combined with any of the other four biomarkers, prediction accuracies consistently exceeded 95% (Extended Data Fig. 3a and Supplementary Table 14). The extreme gradient-boosting model predicted the probability of HCC recurrence for a combination of IF-specific and TC-specific single-biomarker-labelled tiles. Finally, the trained model was tested on an independent cohort of 170 patients with HCC from cohorts 2, 3, 5 and 7.

Next, to assign an integrative score to a patient with HCC with multiple tile measurements from the IF and TC compartments (encoding spatial information) available for the five biomarkers, we developed the TIMES scoring system by integrating spatial and biomarker information in two steps (Fig. 3b). Step 1: we integrated information from combinations of spatially diverse tiles by averaging their recurrence probability predictions. Specifically, for each gene biomarker, we computed the mean and variance of the recurrence probabilities that were originally assigned to each combination of IF-specific and TC-specific tiles (all P_i values in the biomarker's column of the data table in Fig. 3b). Step 2: we integrated the probability summary statistics of the five biomarkers by computing an inverse variance-weighted geometric mean. Specifically, for each patient with HCC, we computed the product of the mean probability values multiplied by the respective inverse variance of all five biomarkers and then calculated the fifth root of the product. This approach generated an integrative TIMES score for a given patient with HCC, which is valued from 0 to 1 (corresponding to increasing HCC recurrence risk) and represented by a penteract (that is, a 5D hypercube, the volume of which is proportional to the score).

Finally, we applied this TIMES scoring system to mIHC data from the 231 patients with HCC across the five cohorts. It is important to note that the TIMES scoring system is currently a research tool and has not been validated for clinical decision-making. Use of the TIMES scoring system should be limited to research settings and should not guide patient treatment decisions without further extensive validation.

Stability analysis of TIMES scoring

To examine whether the TIMES scores would change if they were computed based on a minimal number of tiles in the IF and TC compartments, we conducted a stability analysis. We used a cohort of 240 patients from 3 centres (Anhui Provincial Hospital, Second Affiliated Hospital of Anhui Medical University and Singapore General Hospital). Instead of analysing the entire WSI (100–600 tiles depending on the size of the tissue) as in our current development, here we limited the analysis to only 2 or 3 tiles from each compartment of each patient.

When compared with the original TIMES score obtained from WSI, the new TIMES scores obtained from 2 or 3 tiles demonstrated strong correlations, with Spearman's correlation coefficients of 0.773 ($P < 2.2 \times 10^{-16}$; Extended Data Fig. 4b) and 0.916 ($P < 2.2 \times 10^{-16}$; Extended Data Fig. 4c), respectively; linear regression coefficients were 0.873 ($P < 2.2 \times 10^{-16}$) and 0.991 ($P < 2.2 \times 10^{-16}$), respectively. The high correlation coefficients obtained from the inclusion of only two or three tiles per compartment, rather than a WSI, support the stability of the TIMES scoring system.

Kaplan–Meier survival curves and Cox proportional hazards regression

We applied the Kaplan–Meier method for survival analysis, using the log-rank test to compare the survival outcomes of two groups and determine statistical significance. Variables exhibiting a significance level of $P < 0.05$ in univariate Cox proportional hazards regression analysis were selected for inclusion in the multivariate Cox proportional hazards regression analysis. DFS curves were visualized using GraphPad (v8.0.2), and Cox proportional hazards regression analyses were conducted using the Survival package (v3.4.0) in R[67,68].

We compared our TIMES score against 118 clinical factors (see Supplementary Table 16 for a complete list), collected from tumour morphology, IHC, staging evaluation, biochemistry, MRI, computed tomography and ultrasound assessments, in terms of their associations with DFS and recurrence in HCC, through univariate and multivariate regressions. For example, results for vascular invasion measures (such as microvascular invasion and macrovascular invasion) are shown in Supplementary Tables 26 and 27; results for multiplicity measures of HCC tumour nodules (such as satellite lesion and tumour count) are shown in Supplementary Tables 28 and 29; and results for the abundances of three NK subpopulations ($CD3^-CD57^+$ mature NK cells, $CD3^-CD56^+$ ordinary NK cells and $CD3^-CD16^+CD56^+$ cytotoxic NK cells) are shown in Supplementary Tables 30 and 31.

Furthermore, we stratified patients with HCC into subgroups according to a few selected clinical factors, and found that associations of TIMES scores with DFS and recurrence outcome remained significant. Such clinical factors included HCC aetiology measures (such as hepatitis B virus, hepatitis C virus and viral infections; Supplementary

Table 18), liver fibrosis and cirrhosis (Supplementary Table 19), vascular invasion measures (such as microvascular invasion and macrovascular invasion; Supplementary Table 32), and multiplicity measures of HCC tumour nodules (such as satellite lesion and tumour count; Supplementary Table 33). These comparisons provided evidence for the prognostic value of the TIMES scoring system in HCC stratification.

TCGA data

Clinical information and RNA expression data (raw counts) from the HCC cohorts of TCGA Research Network were downloaded from the cBioPortal (https://www.cbioportal.org/). Using TCGA dataset, we conducted an analysis to examine the association between clinical recurrence status and gene expression.

Cell lines

The human HCC cell line HepG2, acquired from Immocell, was routinely cultured in Dulbecco's modified Eagle's medium (DMEM) supplemented with 10% heat-inactivated fetal bovine serum (HI-FBS; Vivacell). The HepG2 cell line was obtained from Immocell (IM-H038) and is commonly used as a human HCC cell line. The HepG2 cell line was authenticated by STR before use in this study. The authentication test was last performed on 23 July 2024. The cell line was tested for mycoplasma contamination using PCR and was confirmed to be negative for mycoplasma on 15 March 2024. HepG2 is available in the ICLAC database; however, in this study, HepG2 cells were selected due to their high importance as an in vitro model for immune cell migration, particularly concerning NK cell activity in liver tumours. Despite their origin in hepatoblastoma, HepG2 cells exhibit immune response pathways overlapping with those of HCC. This similarity enables meaningful comparisons of tumour–immune interactions. The HepG2 cell line has been widely utilized in NK cell migration studies, yielding valuable insights into tumour immune evasion mechanisms. The HepG2 line has been extensively used in studies of NK cell migration and has provided valuable insights into tumour immune evasion mechanisms.

The mouse HCC cell line H22, sourced from Procell Life Science & Technology, was routinely cultured in RPMI-1640 with 10% HI-FBS. The NK92 cell line was purchased from Procell Life Science & Technology.

NK92 cells with stable NK92$^{OE\text{-}SPON2}$ were established through transduction with a recombinant lentivirus harbouring the pcSLenti-CMV-SPON2-3×FLAG-PGK-Puro-WPRE3 construct (Obio Technology). Stable NK92$^{KD\text{-}SPON2}$ cells were established by transduction with a recombinant lentivirus harbouring the pCLenti-U6-shRNA (SPON2)-CMV-Puro-WPRE construct (Obio Technology), and we achieved a 99% reduction in SPON2 expression (Extended Data Fig. 6g). Empty vector NK92 cell lines (NK92^{EV}) were established by transduction with a recombinant lentivirus harbouring the pcSLenti-CMV-MCS-3×FLAG-PGK-Puro-WPRE3 construct (Obio Technology).

All cell lines were cultured at 37 °C in a humidified atmosphere with 5% CO_2 for in vitro experiments.

Human NK cell enrichment and gene editing

The acquisition of human tissue and blood samples was approved by the Human Ethics Committee of the University of Science and Technology of China (2019-N(H)-121). All patients provided written informed consent. Human primary NK cells were enriched from peripheral blood mononuclear cells (PBMCs) of healthy donors using an NK cell expansion kit (Hangzhou Zhongying Biomedical Technology) according to the manufacturer's instructions, followed by isolation with magnetic-activated cell sorting kits (Miltenyi Biotec). Enriched NK cells, whether gene-edited or control, were maintained in KBM581 medium supplemented with 10% FBS, penicillin and streptomycin (100 U ml^{-1}) plus human IL-2 (200 U ml^{-1}). The medium was changed every 2 days.

NK cells were expanded from human PBMCs and cultured with membrane-bound IL-21 (mbIL21) feeder cells in the presence of 200 U ml^{-1} IL-2 for over 1 week to promote NK cell expansion. To generate *SPON2*-deficient human NK cells, 5×10^6 expanded NK cells were harvested, washed twice with 10 ml of PBS and centrifuged for 5 min at 500*g* and aspiration of PBS. The cell pellet was resuspended in 100 µl of P3 Primary Cell 4D-Nucleofector Solution containing premixed Cas9 (a bacterial RNA-guided endonuclease) and nuclear localization signal (NLS) protein (5 µl at 5 µg µl^{-1}; novoprotein) and preassembled synthetic *SPON2*-targeting single guide RNA (designed to target the *SPON2* open reading frame specifically; 4 µl at 100 µM; sequence: CCACGCCCACGAACCAGUCG; GenScript). After standing for 10 min at room temperature, the cells were electroporated (4D-Nucleofector Core Unit and X Unit) with the EN-138 program, transferred to 3 ml medium, and incubated in a 6-well plate at 37 °C under 5% CO_2. The absence of SPON2 protein expression was confirmed by flow cytometry.

Lentivirus production and NK cell line transduction

HEK293T cells were transfected with Lipofectamine 2000 (Thermo Fisher) and DNA of lentiviral vector (pCDH-CMV-MCS (*Spon2*)-EF1 α-copGFP-T2A-Puro), second-generation packaging plasmid pMD2.G and psPAX2 at a 3:1:2 mass ratio. Six hours post-transfection, media were changed and lentiviral supernatant was collected 3 days later, filtered through a 0.45-mm syringe. Then, lentiviral supernatant was concentrated by centrifugation at 130,000*g* for 1 h 40 min at 4°C. Viral particles were resuspended in PBS at 1/100 of the volume of the total supernatant. Viral titres were determined by serial dilution and transduction of HEK293T cells in the presence of 5 mg ml^{-1} polybrene, and then flow cytometry for GFP expression 3 days later. Expanded NK cells were infected by centrifugation at 1,000*g* for 1 h at an optimal multiplicity of infection of 20 lentiviral particles per cell in a six-well plate containing 2×10^5 cells. Twelve hours post-transfection, media were changed, and infected cells were plated with IL-2 (200 U ml^{-1}) for 2 days.

The resulting NK$^{OE\text{-}SPON2}$ and NK$^{KO\text{-}SPON2}$ cells were then stimulated with 20 ng ml^{-1} of IL-12, 50 ng ml^{-1} of IL-15 and 10 ng ml^{-1} of IL-18 for 1 day, followed by co-culture with CD8$^+$ T cells and HepG2 cells.

Human CD8$^+$ T cell purification

Human CD8$^+$ T cells were isolated from the PBMCs of healthy donors using magnetic-activated cell sorting kits (Miltenyi Biotec). CD8$^+$ T cells (dead$^-$CD45$^+$CD8$^+$CD3$^+$) with a purity exceeding 90% were used in each assay. Flow cytometric data were acquired using a CytoFLEX flow cytometer (Beckman) with CytExpert software and analysed using FlowJo software (v10.7.1; Tree Star).

Flow cytometric analysis

For flow cytometric analyses (human), cells were left untreated or stimulated with 30 ng ml^{-1} phorbol 12-myristate 13-acetate (PMA) and 1 µg ml^{-1} ionomycin, followed by 2.5 µg ml^{-1} monensin (Sigma-Aldrich). After washing with PBS, the cells were stained with a Zombie Aqua Fixable Viability Kit (BioLegend) or a Horizon Fixable Viability Stain 700 (BD Biosciences). The reaction was terminated by washing with PBS containing 1% FBS. Subsequently, the cells were stained for 30 min at 4 °C with fluorophore-conjugated antibodies specific for panels of cell-surface markers. Intracellular staining was performed using the FoxP3/Transcription factor Fix/Perm Kit (eBioscience).

For flow cytometric analyses (mice), cells were stimulated with 30 ng ml^{-1} PMA and 1 µm ionomycin in the presence of 2.5 µg ml^{-1} monensin. After stimulation, the cells were stained with fluorescence-conjugated antibodies specific for surface markers, fixed and permeabilized using the Foxp3/Transcription Factor Staining Buffer Set (eBioscience) in accordance with the manufacturer's protocol. Data were acquired with a CytoFLEX flow cytometer (Beckman) using CytExpert software and analysed with FlowJo software (v10.7.1; Tree Star). Specifics of the antibodies used for flow cytometric analysis can be found in Supplementary Table 25.

Flow cytometric cell cytotoxicity assay

HepG2 cells (1×10^7) in 1 ml PBS were labelled with 5 μM CFSE (Biosharp) at 37 °C for 20 min. Subsequently, the cells were incubated in 5 ml RPMI 1640 (10% FBS) for 10 min at room temperature to deactivate free CFSE. The cells were washed twice and resuspended in RPMI 1640 (10% FBS). Before use in cytotoxicity assays, the viability of CFSE-loaded HepG2 cells was verified through trypan blue staining. NK cells ($NK^{OE\text{-}SPON2}$ or $NK^{KO\text{-}SPON2}$), $CD8^+$ T cells and CFSE-loaded HepG2 cells were co-cultured at a ratio of 3:3:1 (0.6 million:0.6 million:0.2 million) for 4 h in 96-well cell culture plates (200 μl medium per well). To assess cytotoxic activity[69], the cells were washed and stained with 7-AAD and annexin V (Yeasen) according to the manufacturer's instructions. The analysis was performed using a CytoFLEX flow cytometer (Beckman), and the data were analysed with FlowJo software (v10.7.1; Tree Star).

3D-printed tumour organoid model

Sterile PBS was used to prepare the printing prepolymer solution containing 4%/5% Gel-MA, 0.25% HA-MA, 0.25% LAP and 0.05% Lemon Yellow (EFL)[70]. After filtration through a 0.22-μm pore size filter, the solution was stored in the dark at 37 °C. Single-cell suspensions of 5×10^6 ml^{-1} PKH67-prestained HepG2 cells and 1×10^7 ml^{-1} PKH62-prestained NK92 cells were prepared and kept on ice. The printing ink for the inner circle (diameter of 6 mm and thickness of 0.5 mm) of the model representing the tumour area was created by mixing HepG2 cells with 5% Gel-MA, 0.25% HA-MA, 0.25% LAP and 0.05% Lemon Yellow[70]. The printing ink for the outer circle (external diameter of 12 mm, internal diameter of 6 mm and thickness of 0.5 mm) representing the immune area was formulated by mixing NK92 cells with 4% Gel-MA, 0.25% HA-MA, 0.25% LAP and 0.05% Lemon Yellow. The model was printed according to preset conditions using a projection light-curing biological 3D printer (BP8600, EFL).

Subsequently, the printed model was incubated at 37 °C in 50% HepG2 medium (DMEM + 10% FBS + 1% penicillin and streptomycin) and 50% NK92 medium (MEMα + 0.2 mM inositol +0.1 mM β-mercaptoethanol + 0.02 mM folic acid + 100–200 U ml^{-1} recombinant IL-2 + 12.5% horse serum + 12.5% FBS + 1% penicillin and streptomycin), and cell movement was tracked with the fluorescence microscope CytoSMART Lux3 FL (Axion BioSystems). Cell tracking was performed over 5 days at one frame per 30 min. After 5 days, the inner and outer rings were separated, and the cells were lysed with Gel-MA lysis buffer (EFL) for flow cytometric analysis. Cell migration was analysed using the ImageJ TrackMate plugin, supported by manual supervision and verification.

Co-cultures

We investigated the antitumoural mechanism and cell–cell interactions involving SPON2 by performing a series of co-culture experiments involving HepG2 cells, *SPON2*-knockout ($NK^{KO\text{-}SPON2}$) primary NK cells, *SPON2*-overexpression ($NK^{OE\text{-}SPON2}$) primary NK cells and $CD8^+$ T cells. $NK^{KO\text{-}SPON2}$ cells were derived from genetically modified primary human NK cells through CRISPR–Cas9 ribonucleoprotein electroporation, using a *SPON2*-targeting knockout to ablate SPON2 expression, whereas $NK^{OE\text{-}SPON2}$ cells were derived from lentiviral transfection to induce increased SPON2 abundance.

To assess the interactions between $CD8^+$ T cells and $NK^{OE\text{-}SPON2}$ or $NK^{KO\text{-}SPON2}$ cells, isolated $CD8^+$ T cells were co-cultured either directly or indirectly (via transwell plates) with activated $NK^{OE\text{-}SPON2}$ or $NK^{KO\text{-}SPON2}$ cells for 24 h. The co-cultures were performed in the presence of anti-IFNγ (10 ng ml^{-1}) or isotype control antibodies (10 ng ml^{-1}) at a 1:1 ratio (0.2 million:0.2 million). Following the co-culture period, the cells were stained as described above.

NK cell ligand–receptor analysis using single-cell RNA-seq data

For ligand-receptor analysis, we compared the signalling signatures of $SPON2^+$ and $SPON2^-$ NK cells with those of other cells within the TME, utilizing a single-cell RNA-seq dataset. This analysis was performed through tools such as CellChat (v1.1.3) and NicheNet (v1.1.0). Retaining the grouping in the original reports, we divided the cell types in the single-cell sequencing data into $SPON2^+$ NK cells (SPON2 > 0) and $SPON2^-$ NK cells (SPON2 < 0). The cell types considered in the cell interaction analysis encompassed C15_Mey, C17_Endo, C18_Epi, C19_Tcell, C21_pDC, C22_plasma, C23_HSC, C6_B cell, CD4 T, CD8 T, myeloid, $SPON2^-$ NK, $SPON2^+$ NK and tumour cells. In this context, $SPON2^+$ NK cells were treated as target cells, whereas $SPON2^-$ NK cells served as reference cells, enabling the evaluation of the regulatory potential of $CD8^+$ T cells within the tumour immune microenvironment.

Mass cytometry

Mass cytometry experiments were conducted using reagents, instruments and software from Polaris Biology, unless otherwise specified. A detailed list of all mass cytometry antibodies (CytoATLAS) used in the panel setup is provided in Supplementary Table 25.

HCC specimens were minced into small fragments and subjected to enzymatic digestion in RPMI 1640 medium (HyClone Laboratories) supplemented with 1 mg ml^{-1} collagenase IV (Sigma-Aldrich), 150 U ml^{-1} DNase I (Roche) and 5% FBS (HyClone Laboratories) at 37 °C for 1 h. The resulting cell suspension was filtered through a 200-μm mesh to remove undigested tissue fragments. Mononuclear cells were then isolated by Percoll centrifugation, washed and resuspended in RPMI 1640 medium supplemented with 10% FBS. This protocol effectively isolates tumour-infiltrating leukocytes (TILs) while removing most tumour cells, enabling focused analysis of immune cell populations from HCC specimens. For sample staining and acquisition, cells underwent an initial wash with LunaStain cell staining buffer and were treated with 10 μl cisplatin at room temperature for 5 min. After washing with LunaStain cell staining buffer, cells were stained with 5 μl Fc block (BioLegend) for 10 min, followed by a mixture of heavy metal-labelled membrane antibodies for 30 min at room temperature. Subsequently, cells were washed twice with LunaStain cell staining buffer and stained with Ir-DNA intercalator reagent for 10 min. The cells were then washed and adjusted to a concentration of 10^6 ml^{-1} in LunaAcq cell acquisition solution containing 20 μl SureBits element calibration beads. Cell acquisition was conducted at a rate of 800 events per second on a mass cytometer (StarionX1).

The acquired mass cytometry data were normalized and converted into standard FCS 3.0 files (StarionX1). Manual gating was performed using FlowJo (BD Biosciences). UMAP was used to provide an overview of the immune compartment. To identify different cell subtypes, FlowSOM clustering and metaclustering were performed.

Mice

C57BL/6J mice were procured from GemPharmatech, whereas $Spon2^{-/-}$ mice, NK-specific *Spon2*-deficient mice and NOD-*Prkdc*^{scid}*Il2rg*^{em1}/Smoc (M-NSG) immunodeficient mice were obtained from the Shanghai Model Organisms Center. These mice, 6–8 weeks of age, were housed in a specific pathogen-free facility at the University of Science and Technology of China under a 12-h light–12-h dark cycle, with a room temperature of 20–26 °C and relative humidity maintained between 50% and 70%. An irradiation-sterilized mouse diet (WQ JXBIO-TECHNOLOGY) was provided to all experimental mice. All experimental procedures adhered to the National Guidelines for Animal Usage in Research (China) and were approved by the Animal Ethics Committee of the University of Science and Technology of China (USTCACUC25030123013). It is important to note that the maximum tumour size in this study did not exceed the limits set by the Animal Ethics Committee of the University of Science and Technology of China.

Mouse models

To establish mouse HCC models, H22 cells (1×10^7) were injected into the livers of male C57BL/6J mice (7 weeks of age). After 14 days, orthotopic

tumour tissues were obtained, cut into fragments (approximately 3 mm^3) and mixed with Matrigel (0827045, ABW).

Subcutaneous transplantation HCC mouse models. As summarized in Fig. 5a, orthotopic tumour tissues implanted subcutaneously into WT and *Spon2*$^{-/-}$ mice. Tumour measurements were initiated at 5 days post-implantation and continued daily using digital callipers. Tumour volumes (mm^3) were calculated as length (mm) × width (mm) × width (mm) × 0.5. Mice were killed at 18 days post-implantation, and the subcutaneous tumours were removed, cut into small pieces with ophthalmic scissors and resuspended in DMEM containing 1 mg ml^{-1} collagenase IV and 150 U ml^{-1} DNase I. The tumour tissue was digested at 37 °C with shaking (220 rpm) for 40 min until the digestive fluid appeared turbid and was subsequently filtered (200 mesh) before centrifugation at 500*g* for 5 min. The supernatant was discarded, and the lymphocytes were isolated using 40% and 70% Percoll according to the manufacturer's instructions.

Orthotopic transplantation HCC mouse models that simulated tumour immune microenvironment. As summarized in Fig. 5f, orthotopic tumours were prepared as described above and implanted into the livers of WT and *Spon2*$^{-/-}$ mice. Mice were killed at 22 days post-implantation for liver tumour analysis. The hepatosomatic index used to measure tumour development was determined as (tumour weight)/body weight) × 100%[71,72].

Subcutaneous HCC mouse models with NK-specific *Spon2* knockout. As summarized in Fig. 5i, orthotopic tumour tissues were implanted subcutaneously into *Spon2*$^{f/f}$-*Ncr1*$^{Cre+}$ and *Spon2*$^{f/f}$-*Ncr1*$^{Cre-}$ (as a control group) mice. Tumour measurements were initiated at 7 days post-implantation and continued every 2 days using digital callipers. Mice were killed at 22 days post-implantation.

HepG2 mouse models of human HCC with human NK$^{OE\text{-}SPON2}$ or NK$^{KO\text{-}SPON2}$ cells adoptive transfer. As summarized in Fig. 5k, human hepatoma models were established using HepG2 cells in male NSG mice (6–8 weeks of age) lacking T, B and NK cells. For the development of solid tumours, 5×10^6 HepG2 cells were implanted subcutaneously into mice on day −10. After 10 days (day 0), tumour-bearing mice of similar size were randomly divided into three groups ($n = 5$) and PBS or effector cells (5×10^6 NK$^{OE\text{-}SPON2}$ cells or NK$^{KO\text{-}SPON2}$ cells per mouse in PBS) were transferred into the tail vein. To support NK cell survival in vivo, IL-2 (75,000 U) was injected intraperitoneally every 2 days. From day 10, tumour growth was measured every 2 days using digital callipers.

In situ orthotopic HCC mouse models. As summarized in Extended Data Fig. 9a, plasmids Myc-PT3EF1a, Pt/CaggsNRASV12 and PT2/C-Luc/PGK-SB13 (20 μg ml^{-1} in PBS; 100 μl g^{-1} body weight) were transferred into male C57BL/6 mice (8 weeks of age) by hydrodynamic injection into the tail vein[72]. The Myc oncogene is often amplified and overexpressed in human HCC and hepatoblastoma tissues. Mouse liver transfection with Myc leads to tumour formation and lethality in 5–8 weeks. The Ras–MAPK cascade is frequently activated in human HCCs, which can be achieved by using NRasV12 in vivo. The plasmid PT2/C-Luc//PGK-SB13, encoding Sleeping Beauty transposase, expresses firefly luciferase. However, the weakened bioluminescence imaging signals in all groups were probably due to unintegrated plasmid degradation. Mice were killed 35 days after injection ($n = 4$ per group) for liver collection and analysis. All plasmids were gifted from T. Liang's Laboratory.

Subcutaneous HCC mouse models that depleted NK, CD8$^+$ T or both cell types. As summarized in Extended Data Fig. 9i, to assess which immune cells could perform the observed antitumoural effects, NK cells and CD8$^+$ T cells were depleted by intraperitoneal injection of NK antibody (200 μg per mouse) and CD8 antibody (100 μg per mouse) every 3 days for a total of 4 times for 6 days before tumour implantation. H22 cells (3×10^6) were injected subcutaneously into C57BL/6 mice (5–6 weeks of age). Tumour measurements began 7 days after implantation and continued every 2 days with digital callipers. The mice were killed after 21 days.

HepG2 mouse models of human HCC with human NK^{stimulated} cells adoptive transfer. As summarized in Extended Data Fig. 9p, to construct HepG2 mouse models of human HCC through adoptive transfer of human NK cells, 5×10^6 HepG2 cells were implanted subcutaneously into male NSG mice (6–8 weeks of age). After 7 days, 4×10^6 NK^{stimulated} cells (selected from human PBMCs, and stimulated with 250 U ml^{-1} IL-2, 10 ng ml^{-1} IL-15, 10 ng ml^{-1} IL-12, 50 ng ml^{-1} IL-18 or 10 ng ml^{-1} TNF), human NK cells (selected from human PBMCs and stimulated with 200 U ml^{-1} IL-2) or PBS (as a control) were transferred into the tail vein of the mice. To support NK cell survival in vivo, IL-2 (75,000 U) was injected intraperitoneally every other day for approximately seven times, and tumour growth was measured by digital callipers every other day over a 14-day period.

Statistical analysis and reproducibility

Statistical analyses were conducted using GraphPad Prism (v8.0.2), R (v.3.6.1) and RStudio (v.3.5.3). The number of samples (n) used per experiment and the statistical test used are indicated in the figure legends. All in vitro and in vivo experiments were repeated at least twice and always with multiple replicates, except for the following experiments that were performed only once: spatial transcriptomics, IHC and reticulin staining. The 3D-printed tumour organoid model experiment for which representative images are shown were repeated at least three times. Unpaired Student's t-tests were used for unpaired comparisons, whereas paired t-tests were used for paired comparisons. Survival analyses were conducted using log-rank tests. Statistical significance was set at $P < 0.05$.

Ethics statement

This study was approved by Anhui Provincial Hospital (KY2021204 and KY2021212), the Hunan Provincial Cancer Hospital Ethics Committee (JG2019-C485) and the Agency for Science, Technology and Research (A*STAR), IRB: 2021-161 and 2021-188. The collection of human blood was approved by the Human Ethics Committee of the University of Science and Technology of China (2019-N-(H)-121 and 2023-A-(H)-048).

Reporting summary

Further information on research design is available in the Nature Portfolio Reporting Summary linked to this article.

Data availability

The DSP sequencing, LC–MS/MS and 10x Visium data in this study have been deposited in the China National Center for Bioinformation (CNCB) database, under user accession projects OMIX005738, OMIX005736 and HRA006579. The human genome dataset GRCh38 used for 10x Visium data alignment was downloaded from https://www.10xgenomics.com/support/software/space-ranger/downloads. The accession number for the data of single-cell RNA-seq reported in this paper is CNP0000650 (https://db.cngb.org/search/project/CNP0000650). In addition, this study contains Extended Data Figs. 1–10, Supplementary Tables 1–38 and Supplementary Figs. 1–9. In Supplementary Tables 34–37, we reviewed existing clinical guideline on early-stage HCC treatment (Supplementary Table 34), previous comparative research on early-stage HCC treatment (Supplementary Table 35), previous studies on the prognostic value of NK cells in HCC (Supplementary Table 36) and SPON2-related research in fibroblasts (Supplementary Table 37). Source data are provided with this paper.

Code availability

A Code Ocean capsule (https://doi.org/10.24433/CO.7364332.v1) containing executable programming scripts and input and output data is accessible.

46. Zhou, Y. et al. Metascape provides a biologist-oriented resource for the analysis of systems-level datasets. *Nat. Commun.* **10**, 1523 (2019).
47. Zhang, X. et al. CellMarker: a manually curated resource of cell markers in human and mouse. *Nucleic Acids Res.* **47**, D721–D728 (2019).
48. Hu, C. et al. CellMarker 2.0: an updated database of manually curated cell markers in human/mouse and web tools based on scRNA-seq data. *Nucleic Acids Res.* **51**, D870–D876 (2023).
49. Mootha, V. K. et al. PGC-1α-responsive genes involved in oxidative phosphorylation are coordinately downregulated in human diabetes. *Nat. Genet.* **34**, 267–273 (2003).
50. Subramanian, A. et al. Gene set enrichment analysis: a knowledge-based approach for interpreting genome-wide expression profiles. *Proc. Natl Acad. Sci. USA* **102**, 15545–15550 (2005).
51. Lim, J. C. T. et al. An automated staining protocol for seven-colour immunofluorescence of human tissue sections for diagnostic and prognostic use. *Pathology* **50**, 333–341 (2018).
52. Ng, H. H. M. et al. Immunohistochemical scoring of CD38 in the tumor microenvironment predicts responsiveness to anti-PD-1/PD-L1 immunotherapy in hepatocellular carcinoma. *J. Immunother. Cancer* **8**, e000987 (2020).
53. Yeong, J. et al. Prognostic value of CD8$^+$PD-1$^+$ immune infiltrates and PDCD1 gene expression in triple negative breast cancer. *J. Immunother. Cancer* **7**, 34 (2019).
54. Yeong, J. et al. High densities of tumor-associated plasma cells predict improved prognosis in triple negative breast cancer. *Front. Immunol.* **9**, 1209 (2018).
55. Bankhead, P. et al. QuPath: open source software for digital pathology image analysis. *Sci. Rep.* **7**, 16878 (2017).
56. Van Acker, H. H., Capsomidis, A., Smits, E. L. & Van Tendeloo, V. F. CD56 in the immune system: more than a marker for cytotoxicity? *Front. Immunol.* **8**, 892 (2017).
57. Sung, J. J. et al. Immunohistochemical expression and clinical significance of suggested stem cell markers in hepatocellular carcinoma. *J. Pathol. Transl. Med.* **50**, 52–57 (2016).
58. Tsuchiya, A. et al. Hepatocellular carcinoma with progenitor cell features distinguishable by the hepatic stem/progenitor cell marker NCAM. *Cancer Lett.* **309**, 95–103 (2011).
59. Phillips, D. et al. Highly multiplexed phenotyping of immunoregulatory proteins in the tumor microenvironment by CODEX tissue imaging. *Front. Immunol.* **12**, 687673 (2021).
60. Black, S. et al. CODEX multiplexed tissue imaging with DNA-conjugated antibodies. *Nat. Protoc.* **16**, 3802–3835 (2021).
61. Wu, H. et al. Postmortem high-dimensional immune profiling of severe COVID-19 patients reveals distinct patterns of immunosuppression and immunoactivation. *Nat. Commun.* **13**, 269 (2022).
62. Li, R. et al. A body map of somatic mutagenesis in morphologically normal human tissues. *Nature* **597**, 398–403 (2021).
63. Emmert-Buck, M. R. et al. Laser capture microdissection. *Science* **274**, 998–1001 (1996).
64. Deng, M. et al. Proteogenomic characterization of cholangiocarcinoma. *Hepatology* **77**, 411–429 (2023).
65. Schwanhäusser, B. et al. Global quantification of mammalian gene expression control. *Nature* **473**, 337–342 (2011).
66. Li, T. et al. TIMER2.0 for analysis of tumor-infiltrating immune cells. *Nucleic Acids Res.* **48**, W509–W514 (2020).
67. Andersen, P. K. & Gill, R. D. Cox's regression model for counting processes: a large sample study. *Ann. Stat.* **10**, 1100–1120 (1982).
68. Therneau, T. M. & Grambsch, P. M. Modeling survival data: extending the Cox model. *Stat. Biol. Health* https://doi.org/10.1007/978-1-4757-3294-8 (2000).
69. Li, J. et al. Biodegradable electrospun nanofibrous platform integrating antiplatelet therapy–chemotherapy for preventing postoperative tumor recurrence and metastasis. *Theranostics* **12**, 3503–3517 (2022).
70. Tang, M. et al. Three-dimensional bioprinted glioblastoma microenvironments model cellular dependencies and immune interactions. *Cell Res.* **30**, 833–853 (2020).
71. Wu, Y. et al. Blockade of T-cell receptor with Ig and ITIM domains elicits potent antitumor immunity in naturally occurring HBV-related HCC in mice. *Hepatology* **77**, 965–981 (2023).
72. Xu, X. et al. Group-2 innate lymphoid cells promote HCC progression through CXCL2-neutrophil-induced immunosuppression. *Hepatology* **74**, 2526–2543 (2021).

Acknowledgements This work was supported by the National Key R&D Program of China (2021YFC2300604 and 2022YFA1303200), the National Natural Science Foundation of China (82394452, 82022056, 92169118, 82222048, 32330062, 82373232 and 32470720), the CAS Project for Young Scientists in Basic Research (grant no. YSBR-068), the Natural Science Foundation of Anhui Provincial (2008085J35 and 2408085JX013), the A*STAR Biomedical Engineering Programme (C211318003), the Singapore National Medical Research Council (MOH-000323-00 and OFYIRG19may-0007), the Industry Alignment Fund-Industry Collaboration Fund (IAF-ICP I2201E0014), the Central Public-interest Scientific Institution Basal Research Fund (no. 1102431600020230001) and the Qingyun Project Research Fund (PB- KC012101). We thank L. Sun, H. Sun and Z. Tian for their invaluable assistance, support, guidance and contributions to this study; T. Liang for generously providing the plasmid used in this research; and Y. Wang, M. Xiao and X. Wang for their assistance with the mass cytometry assays.

Author contributions C.S., L.L. and J.Y. conceived and directed the study. G.J. designed the overall data analysis strategies and developed the artificial intelligence approaches. L.L., J.W., J.C.T.L., Y.L., W.W., Y.Z., B.N. and Y.L. collected clinical samples for paraffin embedding. P.H. and F.L. performed the 10x Genomics Visium profiling and analysis. C.D. and F.L. conducted the proteomic analysis. P.H., F.L. and S.H. performed the Nanostring DSP profiling and analysis. G.J. and S.H. constructed the machine learning models using the transcriptomics data and developed the TIMES scoring system using the proteomics data. F.W., P.H., F.L., G.J. and S.H. performed the mIHC. G.J., T.L.K.H., N.-T.N., J.W., F.W., F.L., P.H. and S.H. validated the TIMES scoring system. P.H. analysed the single-cell RNA-seq data. P.H. and M.S. conducted the PhenoCycler mapping and analysis. M.S. and Q.T. established the 3D-bioprinting model. P.H. and F.W. performed the mIHC studies and survival analysis. T.D. conducted the mouse model studies. P.H. and A.U. built the TIMES website. C.S. and L.L. supervised the research. C.S., G.J. and D.G. drafted and revised the manuscript. All authors approved the final version of the manuscript.

Competing interests The authors declare no competing interests.

Additional information

Supplementary information The online version contains supplementary material available at https://doi.org/10.1038/s41586-025-08668-x.

Correspondence and requests for materials should be addressed to Joe Yeong, Lianxin Liu or Cheng Sun.

Peer review information *Nature* thanks George Miller, Christian Schürch and the other, anonymous, reviewer(s) for their contribution to the peer review of this work. Peer reviewer reports are available.

Reprints and permissions information is available at http://www.nature.com/reprints.